

This is an Open Access document downloaded from ORCA, Cardiff University's institutional repository:<https://orca.cardiff.ac.uk/id/eprint/170440/>

This is the author's version of a work that was submitted to / accepted for publication.

Citation for final published version:

Wei, Sheng-Jie, Cleall, Peter J. , Chen, Yun-Min and Li, Yu-Chao 2024. All-atomic modelling of the compaction of montmorillonite clays: fabric evolution and energy conversion. *Journal of Geotechnical and Geoenvironmental Engineering*

Publishers page:

Please note:

Changes made as a result of publishing processes such as copy-editing, formatting and page numbers may not be reflected in this version. For the definitive version of this publication, please refer to the published source. You are advised to consult the publisher's version if you wish to cite this paper.

This version is being made available in accordance with publisher policies. See <http://orca.cf.ac.uk/policies.html> for usage policies. Copyright and moral rights for publications made available in ORCA are retained by the copyright holders.



All-atomic Modelling of the Compaction of Montmorillonite Clays: Fabric Evolution and Energy

Conversion

Sheng-Jie Wei,¹ Peter J. Cleall, Ph.D.,² Yun-Min Chen, Ph.D.,³ and Yu-Chao Li, Ph.D.⁴

¹Ph.D. Candidate, Minister of Education Key Laboratory of Soft Soils and Geoenvironmental Engineering, Department of Civil Engineering, Zhejiang University, Hangzhou 310058, China; email: sheng-jie_wei@zju.edu.cn

²Professor, School of Engineering, Cardiff University, Cardiff, U.K.; email: cleall@cardiff.ac.uk

³Professor, Minister of Education Key Laboratory of Soft Soils and Geoenvironmental Engineering, Department of Civil Engineering, Zhejiang University, Hangzhou 310058, China; email: chenyunmin@zju.edu.cn

⁴Professor, Minister of Education Key Laboratory of Soft Soils and Geoenvironmental Engineering, Department of Civil Engineering, Zhejiang University, Hangzhou 310058, China; email: liyuchao@zju.edu.cn (Corresponding author)

ABSTRACT

Compaction is an essential compression process for sedimentary soils. Compared to in-depth studies on granular soil behaviors, numerical modelling of clay compaction is still in its infancy. This study presents

an all-atomic modelling framework to investigate the compaction of anhydrous montmorillonite from initially fully exfoliated platelets. The total number of inter-particle contacts increased and the meso-pores were dominant during the formation of card-house structures. As the local fabrics evolved to book-house structures, the contact evolutions became predominant and partial meso-pores transformed into micro-pores. The coordinated deformations during the formation of compacted aggregates dramatically increased inter-particle contacts and so the micro-pores became dominant. After rebound, the inter-particle contacts decreased and partial micro-pores were restored. The total potential energy decreased during contact evolutions due to the significant reduction in interaction potential energy between clay particles, while hysteresis was observed during coordinated deformations and rebound due to the changes in internal potential energy within deformed clay particles. The internal potential energy was primarily determined by the electrostatic forces except under significant deformations, where the van der Waals forces became dominant. The interaction potential energy remained unchanged with specific contact types, but decreased significantly due to electrostatic interaction when contacts evolved. As computational capacity develops, a greater number of larger hydrated clay particles can be used to improve simulations of compaction and other macroscopic behaviors via all-atomic molecular dynamics simulations.

AUTHOR KEYWORDS

Molecular dynamics; Clay; Compaction; Fabric; Potential energy

1 INTRODUCTION

2 Compaction, mainly by expelling air from voids (Benhamida et al. 2005), is an essential compression
3 process for soil sedimentary. The evolution history of fabrics and interactions during compaction shows
4 significant influences on the response of soils in the subsequent engineering applications (Tarantino and
5 De Col 2008). Changes in the interactions between particles under external loads result in fabric evolutions
6 via the rotation, translation and deformation of particles, which consequently lead to the compaction of
7 soils. Therefore, quantitative descriptions of fabric evolution and inter-particle interactions can help to
8 interpret the compaction behavior of soils from particle-scale.

9 For granular soils (e.g., sands), particle-scale behavior is governed by contact forces (i.e., skeletal force)
10 (Santamarina 2003). The fabric evolutions induce changes in the internal-anisotropic contact network,
11 which plays an important role in the compaction of granular soils (Imseeh et al. 2018). Observational
12 imaging techniques, such as X-ray computed tomography (Zhao et al. 2015) and scanning electron
13 microscope (Santagata et al. 2014), have been used to demonstrate the relationships between particle
14 morphology (Nie et al. 2021), fabric evolution (Cheng and Wang 2018), and their influences on the
15 compaction of granular soils (Yin et al. 2023). Due to the multi-scale characteristic lengths of granular soils
16 (Xiong et al. 2022), it is challenging to explore impacts of a single variable merely via observational imaging
17 techniques. The discrete element method (DEM) has been employed as a numerical simulation approach
18 to investigate granular soil behaviors (Cundall and Strack 1979; Zhao and Guo 2013), because it allows for
19 the control of target parameters and continuous monitoring of fabric (Jiang 2019). The DEM framework
20 for granular soils, especially the contact constitutive models, was summarized to establish the benchmark

21 of particulate simulations (O'Sullivan 2011), and it was used to simulate fabric evolution under different
22 loading conditions (Vijayan et al. 2020). These simulations revealed that an increase in the coordination
23 number of soil particles densified the contact network to bear the increasing loading stresses (Gu et al.
24 2015), and the contact evolutions along the principle stress direction contributed to the hysteretic effect
25 (Vijayan et al. 2020).

26 There is however a significant difference in the inter-particle mechanics of granular soils and clay (swelling
27 clay in particular). Clay particles have a large specific surface area (van Olphen 1977) and high surface
28 chemical activity, making the influences of non-contact forces (i.e., van der Waals force, electrostatic force,
29 etc.) between clay particles significant. Hence, the particle-scale behavior of clay is controlled by both
30 contact and non-contact forces (Pedrotti and Tarantino 2018). The factors affecting non-contact forces are
31 highly complex and dependent on mineral structure, charge density and pore media characteristics.
32 Moreover, flat clay particles are prone to deformations with low rigidity (Honorio et al. 2018), which is in
33 stark contrast to granular soil particles. Various morphologies can be formed under different
34 environmental conditions, including single crystal layers, quasi-crystals and aggregates (Quirk and Aylmore
35 1971). To address these challenges, numerical simulations have become a valuable way for demonstrating
36 clay compaction, particularly with the development of computational capacity.

37 DEM for clays differs significantly from DEM for granular soils in both model construction and force field
38 selection. Straight line segments were proposed as discrete element models for clay particles (Fig. 1(a))
39 and hinged nodes were set to approximate particle bending (Anandarajah 1994). Compression behavior
40 was simplified as a two-dimensional (2D) problem (Anandarajah and Lu 1991) and described by

41 mechanical contact, double-layer repulsive and van der Waals attractive forces (Anandarajah 1994). This
42 modelling framework allowed exploration of the relationships between particle behaviors and
43 macroscopic characteristics for clays with low computation costs. Anadarajah's framework has
44 subsequently been modified and extended to three-dimensional problems with 3D-blocks (Yao 2002), and
45 used to simulate the compression of kaolinite (Khabazian et al. 2018; Jaradat and Abdelaziz 2019; Pagano
46 et al. 2020) and montmorillonite (Bayesteh and Mirghasemi 2013) respectively, with a particular focus on
47 the impacts of initial orientation arrangements and ion concentrations. In the recent years, more and more
48 researchers attempted to modify the calculation method of inter-particle forces in DEM. A DLVO-based
49 interaction model, calibrated by the Atomic Force Microscope (AFM) force measurement (Guo and Yu
50 2017), was employed to study the suspension structure of kaolinite in terms of particle orientations and
51 contact numbers (Guo and Yu 2019). A simplified linear force model was adopted to approximate the
52 conventional non-linear interactions and reduce the computational costs in the consolidation simulations
53 of kaolinite (Jaradat and Abdelaziz 2023). A multifaceted interaction model with a specified "pull-off force"
54 between attractive surfaces was proposed (de Bono and McDowell 2023a) to simulate the compression
55 and shearing of kaolin clay (de Bono and McDowell 2023b). However, several challenges remained. The
56 2D-lines with hinged nodes could not simulate the conversion of internal potential energy, while the rigid
57 3D block-shaped particles neglected deformations of clay particles. Additionally, the homogeneous nature
58 of discrete elements could not completely account for the non-homogeneous distribution of clay particle
59 charges caused by isomorphous substitutions and the (de-)protonation of edges. As for inter-particle
60 interactions, since current experimental techniques were unable to directly calibrate model parameters,
61 the approximate methods to calculate repulsive electrostatic force (Lu and Anandarajah 1992) and

62 attractive van der Waals force (Anandarajah and Chen 1995) between two inclined finite particles in DEM
63 were not valid for clays with high surface potential (e.g. montmorillonite) (Bayesteh and Mirghasemi 2013)
64 and easily resulted in errors dependent on particle sizes and inter-particle distances (Chen and
65 Anandarajah 1996).

66 Coarse-grained (CG) simulation method (Suter et al. 2009; Bandera et al. 2021) is an efficient method to
67 perform particle-scale simulations of clay and has also been used to investigate clay agglomeration
68 (Ebrahimi et al. 2016a; Zhu et al. 2019) and compaction (Sjoblom 2016). Each clay particle was modelled
69 by an ellipsoid (Fig. 1(b)), or an assembly of two types of beads (Fig. 1(c)), which represented the main
70 structure and edge of clay particles, respectively. Simulation results successfully revealed the influence of
71 contact number on clay stiffness and clarified that the reorientation during unloading and reloading was
72 the main cause of the hysteresis effect (Sjoblom 2016). However, the CG models were generally rigid and
73 incapable of simulating particle deformations within particles, and the CG simulation method also faced
74 challenges in accurately describing inter-particle interactions. Interactions among CG particles were
75 usually implemented by the DLVO model (Sjoblom 2016; Aminpour and Sjoblom 2019) or other CG force
76 fields (e.g. Gay-Berne potential calibrated by all-atomistic molecular dynamics simulations) (Ebrahimi 2014;
77 Schaettle et al. 2018). The DLVO model may overestimate the electrostatic repulsive force near the surface
78 and neglected the attractive force at the positive-charged edges, resulting in a tendency for dispersion
79 rather than flocculation (Ebrahimi et al. 2014). CG models with Gay-Berne potential (Gay and Berne 1981;
80 Everaers and Ejtehadi 2003) could not simultaneously reflect two free energy valleys of face-face
81 interaction between Na-montmorillonite particles and overestimated the edge-edge interaction at short

82 distance (Ebrahimi et al. 2014; Ebrahimi et al. 2016b).

83 All-atomic modelling for clays became feasible (Cygan et al. 2021) with the development of a general force
84 field for clay minerals, termed CLAYFF (Cygan et al. 2004), which enabled the investigation of clay
85 compaction by all-atomic molecular dynamics (MD) simulations (Fig. 1(d)). All-atomic clay models could
86 describe the local characteristics in mineral structures and charge distributions, and reflect the
87 deformations of flexible clay particles. Combined with laboratory tests and microscopic observations, all-
88 atomic MD simulation reproduced the compaction process of clay aggregates and proposed a prediction
89 model for cohesive energy density (Ahmed and Abduljauwad 2017). Researchers also explored the
90 compaction and dehydration process of clay-like nanoparticle aggregates (Ho et al. 2017; Underwood and
91 Bourg 2020) with all-atomic models, showing the influences of drainage rate and water content on fabric,
92 thermodynamics and mechanical properties, which verified the effectiveness of all-atomic MD simulations
93 in modelling clay behaviors. However, current all-atomic MD simulations mainly focused on the geometric
94 descriptions of fabric evolutions and their influences, lacking analysis of the nanoscale mechanical
95 motivations behind these evolutions.

96 This study presents an all-atomic MD modelling framework to investigate clay compaction from the views
97 of fabric evolution and potential energy conversion. The all-atomic clay models, simulation force field and
98 analysis methods are introduced. In the following section, the fabric evolution is quantitatively described by
99 orientation order parameter, variations of inter-particle contacts, pore size distribution and pore space
100 tomography. The laws of potential energy conversion and dissipation in clays are analyzed by potential
101 energy density calculations. The internal potential energy within a typical particle and interaction potential

102 energy between two typical particles are investigated in terms of electrostatic and van der Waals terms
103 for different stages in the compact-rebound process.

104 **MODEL AND METHOD**

105 In this study, to model the fabric evolution of clay during the compact-rebound process at atomistic-scale,
106 an assembly of clay particles are considered within a contained volume. The particles are modelled at the
107 atomic level using the open-source software LAMMPS (Thompson et al. 2022), with inter-atomic force
108 field described in the following.

109 **Molecular models**

110 An all-atomic clay particle model was constructed following the approach of Ho et al. (2017). In this study,
111 Na-montmorillonite (Na-MMT) with stoichiometry of $\text{Na}_{0.75}\text{Si}_8[\text{Al}_{3.25}\text{Mg}_{0.75}]\text{O}_{20}(\text{OH})_4$ was selected as the
112 representative clay mineral. Initially, a crystalline layer with dimensions of 13.73 nm × 11.88 nm × 0.92 nm
113 was created using the unit cell structure of pyrophyllite proposed by Skipper et al. (1995). The crystalline
114 layer was then cleaved into a hexagonal particle (Underwood and Bourg 2020) with an edge length of 6.86
115 nm along the main growth directions of phyllosilicate crystal chain ([0 1 0], [1 1 0] and [1 -1 0]) (White and
116 Zelazny 1988), as depicted in Fig. 2(a). The undercoordinated oxygen atoms exposed at the edges were
117 healed with hydrogen atoms in neutral-pH environment (Martins et al. 2014; Lavikainen et al. 2015).
118 Isomorphous substitutions were performed by randomly replacing aluminum atoms at the octahedral
119 sheets with magnesium atoms, following the Lowenstein's Law (Lowenstein 1954). This resulted in a
120 permanent charge of -196e ($e = 1.602 \times 10^{-19}$ C) and a surface charge density of -0.128 C/m² in a clay particle,
121 which conformed to the experimental results (-0.193 – -0.125 C/m²) (Sperry and Peirce 1999). To maintain

122 overall electroneutrality, those negative charges were compensated by sodium ions (Na⁺). Unlike earlier
 123 rigid particle models for montmorillonite (Ebrahimi et al. 2014; Kang et al. 2020), the clay particles in this
 124 study are flexible and capable of deformations. Subsequently, 100 clay particles, each of which consisted
 125 of about 10 thousand atoms, were randomly placed in a 70.8-nm cubic simulation box, forming a loose
 126 packing with a void ratio of 30.0 to prevent particle overlapping in the initial model, as illustrated in Fig.
 127 2(b). It is noteworthy that a parametric study with 200 clay particles was also conducted to investigate the
 128 influences of model size. The results indicated that variation laws of fabric evolution and energy conversion
 129 during the compact-rebound process were model size independent.

130 Force field parameters and simulation details

131 The inter-atomic interaction force field in this study referred to the widely-used CLAYFF (Cygan et al. 2004),
 132 which has been successfully employed to simulate clay mineral systems (Mazo et al. 2008; Anoukou et al.
 133 2015; Prishchenko et al. 2018; Cygan et al. 2021; Zhu et al. 2021). The total potential of the system U^{total} ,
 134 consisted of the non-bonded interaction potential $U^{\text{non-bonded}}$, and the bonded interaction potential U^{bonded} .
 135 The former included Coulombic electrostatic interaction U^{Coul} , and van der Waals interaction U^{vdW} . The
 136 latter was composed of a bond-stretching term U^{bond} , and an angle-bending term U^{angle} :

$$137 \quad U^{\text{total}} = U^{\text{non-bonded}} + U^{\text{bonded}} = U^{\text{Coul}} + U^{\text{vdW}} + U^{\text{bond}} + U^{\text{angle}} \quad (1)$$

$$138 \quad U^{\text{Coul}} = \frac{e^2}{4\pi\epsilon} \sum_{i \neq j} \frac{q_i q_j}{r_{ij}} (r_{ij} \leq r_c) \quad (2)$$

$$139 \quad U^{\text{vdW}} = \sum_{i \neq j} 4\epsilon_{ij} \left[\left(\frac{\sigma_{ij}}{r_{ij}} \right)^{12} - \left(\frac{\sigma_{ij}}{r_{ij}} \right)^6 \right] (r_{ij} \leq r_c) \quad (3)$$

140
$$U^{\text{bond}} = D_0 \left\{ 1 - \exp \left[-\alpha (r_{ij} - r_0) \right] \right\}^2 \quad (4)$$

141
$$U^{\text{angle}} = k_0 (\theta_{ijk} - \theta_0)^2 \quad (5)$$

142 The cutoff distance r_c for the short-range part of non-bonded interaction was 1.0 nm. The short-range part
 143 of U^{Coul} was given by Coulombic law, where ϵ is the dielectric constant and q is the atomistic partial charge,
 144 while the long-range part of U^{Coul} was calculated by Particle-Particle and Particle-Mesh (PPPM) solver
 145 (Hockney and Eastwood 1989). Most of the atomistic partial charges were obtained from quantum
 146 chemistry calculation as described in CLAYFF, but the partial charges of edge oxygen atoms were re-
 147 assigned due to the (de-)protonated process at the edges (Lammers et al. 2017). The short-range U^{vdW} was
 148 calculated by Lennard-Jones potential, where ϵ_{ij} ($=\sqrt{\epsilon_i \epsilon_j}$) and σ_{ij} ($=(\sigma_i + \sigma_j)/2$) are energy parameter
 149 and distance parameter between atom i and atom j , respectively. It includes a repulsive term (i.e., r^{-12} term,
 150 referring to Pauli repulsion) and an attractive term (i.e., r^{-6} term, referring to London dispersion) (Wang et
 151 al. 2020). Only the bond-stretching terms of hydroxyl groups were considered, where D_0 is the energy
 152 constant, α is the damping parameters and r_0 is the equilibrium length of bonds in hydroxyl groups. The
 153 angle-bending terms between the metal atoms and the hydroxyl groups (Metal-O-H) were described by
 154 harmonic function, where k_0 is the force constant and θ_0 is the equilibrium angle of Metal-O-H (Cygan et al.
 155 2004). These parameters were empirically derived from experimental data of mineral crystal structures
 156 (Pouvreau et al. 2017; Pouvreau et al. 2019). Besides, to ensure the stability of clay particle models in long-
 157 term MD simulations, additional angle-bending potential with a large force constant ($k_0 = 800 \text{ kcal}\cdot\text{mol}^{-1}$
 158 $\cdot\text{rad}^{-2}$) was assigned to the Metal-O-Metal groups at the edges. (Ho et al. 2017) Detailed force field
 159 parameters are listed in the Supplementary Materials.

160 The analyses for the all-atomic MD simulations, which were undertaken on Intel(R) Xeon(R) Gold 6226R
161 CPUs (2.90 GHz), involved three steps: initial structure optimization, compaction and rebound. First, the
162 loose packing (Fig. 2(b)) was energy-minimized to obtain an optimized structure. The system temperature
163 was then set to 10 K to reduce the thermodynamic fluctuations, and the initial velocities of atoms were
164 assigned based on a Gaussian distribution. After eliminating the initial stress in the model with an anneal
165 simulation under canonical ensemble (NVT, with constant particle numbers, volume and temperature),
166 the isothermal-isobaric ensemble (NPT, with constant particle numbers, pressure and temperature) was
167 applied with an isotropic pressure $P = 1$ atm in three dimensions of the simulation box until the size of the
168 simulation box reached a stable state. The obtained model (43.7 nm \times 44.4 nm \times 32.2 nm), with a void
169 ratio e_0 of about 4.45 and a dry density ρ_{d0} of about 0.50 g/cm³, was regarded as the initial state for the
170 compact-rebound simulation. Subsequently, one-dimensional compaction was performed at a rate of 0.02
171 nm/ps along the z-dimension, while the x and y dimensions remained fixed. This compaction rate was
172 selected to reduce the sampling errors and avoid the influences of overfast relative movements of particles
173 on fabric evolution. The atom positions were remapped according to the changing size of the simulation
174 box under the NVT ensemble. The compaction continued until ρ_d reached 1.98 g/cm³, and the maximum
175 simulated pressure reached about 17.4 MPa, which slightly exceeded static compaction or geological
176 pressure (0.01 GPa), but was far inferior to dynamic compaction pressure (1 GPa) (Ahmed and
177 Abduljauwad 2017). After compaction, the rebound simulation was performed inversely. An equilibrium
178 period of 1 ns and a sampling period of 0.5 ns were conducted after each step of compaction and rebound.
179 The entire compact-rebound simulations lasted for about 40 ns.

180 A time step of 1.0 fs was used, and periodic boundary conditions (Frankel and Smit 2002) were applied to
181 each boundary surface of the domain. System equilibrium criterion was based on the stricter
182 thermodynamics equilibrium condition as opposed to a mechanical equilibrium condition chiefly used in
183 DEM simulations. Throughout the compact-rebound process, thermodynamics properties were monitored
184 to ensure the system had reached a thermodynamic equilibrium state after each equilibrium period.

185 The compact-rebound process was quantitatively analyzed in terms of fabric and energy. According to the
186 definition from Mitchell and Soga (2005), the term “fabric” refers to the arrangement of particles, particle
187 groups, and pore spaces. In our study, the correlation parameter between the particle normal vector and
188 the positive direction of z-axis (i.e., the orientational order parameter) S_z (Allen and Tildesley 2017) was
189 calculated to represent the arrangement of particles; the variations of inter-particle contacts were
190 investigated to reflect the arrangement of particle groups since the contact between two clay particles
191 was the fundamental part of particle groups; the pore size distribution (PSD) and pore space tomography
192 were presented to manifest the arrangement of pore spaces.

193 The singular value decomposition (SVD) algorithm (Arun et al. 1987) was first adopted to match the point
194 sets of atoms and obtain the normal vector \mathbf{n} of particle surface (Supplementary Materials). With the
195 obtained normal vectors of particles, S_z could be calculated as follows:

$$196 \quad S_z = \frac{1}{N_p} \sum_{i=1}^{N_p} \left[\frac{3 \mathbf{n}_i \cdot \mathbf{e}_z^2 - 1}{2} \right] \quad (6)$$

197 where $N_p = 100$ is the total number of clay particles and \mathbf{e}_z is the unit vector of z-direction. For randomly-
198 aligned clay sample, the normal vectors of particles are independent of the z-direction and $S_z = 0$; for

199 transverse-isotropic clay sample, the normal vectors of particles are parallel to the z-direction and $S_z = 1$.

200 Six basic types of inter-particle contacts were considered according to the contact sites and particle
201 morphologies: Vertex-Vertex (VV), Vertex-Edge (VE), Vertex-Face (VF), Edge-Edge (EE), Edge-Face (EF) and
202 Face-Face (FF) contacts, as shown in Fig. 3. A recognition algorithm was developed based on the geometric
203 criteria for different types of contacts (Supplementary Materials). The numbers of inter-particle contacts
204 were then compiled via the algorithm and the average contact numbers per particle (CN) were calculated
205 to avoid the impact of system size. Specifically, two particles with $|\mathbf{n}_i \cdot \mathbf{n}_j| \geq 0.97$ could be regarded as parallel;
206 otherwise, two inclined clay particles were in contact if the minimum distance between octahedral metal
207 atoms d_s was smaller than 1.5 nm. According to the stability analysis in Supplementary Materials, the rank
208 of stability for different contact types was as follows: FF > (EF > VE > EE) > (VF > VV). In this paper, the
209 evolution of inter-particle contacts refers to the transformation from low-stability contacts to high-stability
210 contacts, while degeneration refers to the reverse process.

211 To analyze the pore size distribution (PSD) of clay, pore diameter D at any given point $P(x_p, y_p, z_p)$ was
212 defined as the maximum diameter of a sphere that encompassed point P without overlapping neighboring
213 atoms (Bhattacharya and Gubbins 2006) (refer to Fig. S3(a) for a schematic graph). The detailed calculation
214 method is given in the Supplementary Materials. To visualize the morphologic changes of pore space, the
215 simulation box was divided into a cubic grid with a side length of about 0.15 nm and the space state of
216 each grid cell was determined based on the distances between the center of grid cell and atoms in the
217 system. To ensure a smooth transition between pore space and non-pore space, a Gaussian function was
218 adopted as a switching function (Supplementary Materials) (Lu and Chen 2012). Finally, the software Visual

219 Molecular Dynamics (VMD) (Humphrey et al. 1996) was utilized to generate a contour map of the space
 220 state of each grid cell, which represented the tomography of pore space.

221 The fabric evolution induced potential energy conversion. In order to assess the stability of clay fabrics
 222 under different dry densities, the variations in total potential energy stored within a unit volume of clay
 223 (i.e., total potential energy density) compared to the initial state with $\rho_{d0} = 0.50 \text{ g/cm}^3$, $\Delta\Omega_{\text{sys}}$, was taken as
 224 a characterization parameter. During the sampling period, the total potential energy U^{total} and volume of
 225 clay V were collected, and $\Delta\Omega_{\text{sys}}$ could be calculated as:

$$226 \quad \Delta\Omega_{\text{sys}} = \Delta\Omega_{\text{in}} + \Delta\Omega_{\text{ia}} = \left\langle \frac{U^{\text{total}}}{V} \right\rangle - \left\langle \frac{U_0^{\text{total}}}{V_0} \right\rangle \quad (7)$$

227 where U_0^{total} is the total potential energy of the initial system, V_0 is the initial volume of clay and the notation
 228 $\langle \rangle$ represents the ensemble-averaged value of variables. $\Delta\Omega_{\text{sys}}$ could be further decomposed into the
 229 variations in internal potential energy density within clay particles $\Delta\Omega_{\text{in}}$ and interaction potential energy
 230 density between clay particles $\Delta\Omega_{\text{ia}}$.

231 As for potential energy conversion of a single particle, variations in internal potential energy $\Delta u_{\text{in}}^{\text{total}}$ and
 232 interaction potential energy $\Delta u_{\text{ia}}^{\text{total}}$ were analyzed. $\Delta u_{\text{in}}^{\text{total}}$ was comprised of a Coulombic electrostatic term
 233 $\Delta u_{\text{in}}^{\text{Coul}}$, a van der Waals term $\Delta u_{\text{in}}^{\text{vdW}}$ and a bonded term $\Delta u_{\text{in}}^{\text{bonded}}$. It was dependent on the deformations of
 234 each particle; thus, an index K was defined to quantify the deformations of particles along their normal
 235 vector with respect to their initial undeformed state:

$$236 \quad K = \sum_{i=1}^N \delta_{zi}^2 \quad (8)$$

237 where δ_{z_i} is the deflection of the i^{th} octahedral metal atom in the deformed particle (see Supplementary
238 Materials for a schematic diagram) and N is the total number of octahedral metal atoms in the particle. A
239 larger value of K indicated a greater particle deformation along the normal vector and a larger value of
240 $\Delta u_{ia}^{\text{total}}$. Similarly, $\Delta u_{ia}^{\text{total}}$ included a Coulombic electrostatic term $\Delta u_{ia}^{\text{Coul}}$ and a van der Waals term $\Delta u_{ia}^{\text{vdW}}$.

241 **FABRIC EVOLUTION**

242 Typical states in the simulated compact-rebound process were shown in Fig. 4. Particles were initially
243 scattered with large voids between them and were randomly-aligned with respect to the z-direction (Fig.
244 4(a), $P = 0.1$ MPa, $\rho_d = 0.50$ g/cm³). Particles gradually approached each other under external pressure,
245 leading to a reduction in inter-particle distances (Fig. 4(b), $P = 0.6$ MPa, $\rho_d = 0.89$ g/cm³). The ensuing
246 compaction led to the increase of the number of parallel-stacked particles and the normal vectors of
247 particles tended to align with the compaction direction (Fig. 4(c), $P = 1.4$ MPa, $\rho_d = 1.33$ g/cm³). Further
248 compaction caused the coordinated deformations between particles, leading to a transverse-isotropic clay
249 system (Fig. 4(d), $P = 17.4$ MPa, $\rho_d = 1.98$ g/cm³), which was similar to the soil layers after geological
250 sedimentation. After unloading, there was a slight recovery with layered structure being maintained, and
251 partial small pores recovered (Fig. 4(e), $P = 63.1$ kPa, $\rho_d = 1.63$ g/cm³). A video of the entire simulated
252 compact-rebound process and the loading/unloading curve in the e - $\log(P)$ space are provided in the
253 Supplementary Materials (see Fig. S2).

254 As shown in Fig. 5, S_z increased stepwise from 0.02 to 0.48 as the compaction progressed. The maximum
255 S_z was smaller than the observed value (0.70) in the orientation test of the hydrated Na-montmorillonite
256 (Carrier et al. 2016). At Stage A ($\rho_d < 0.89$ g/cm³), S_z dramatically increased to 0.23, indicating that the

257 interaction between scattered particles played an important role in guiding the rotation of particle normal
258 vectors. At Stage B ($0.89 \leq \rho_d < 1.33 \text{ g/cm}^3$), the Pauli repulsion between particles inhibited the further
259 orientational rotation of clay particles (Underwood and Bourg 2020), resulting in a slow increment of S_z .
260 At Stage C ($1.33 \leq \rho_d < 1.98 \text{ g/cm}^3$), S_z continuously increased to 0.48 due to the rotations and transversely
261 slides between particles during the coordinated deformations within the parallel-stacking particles. At
262 Stage D ($1.98 \geq \rho_d > 1.63 \text{ g/cm}^3$), S_z decreased gradually with the recovery of elastic particle deformations,
263 and the value after rebound was slightly smaller than that before rebound under identical dry density,
264 which suggested that partial orientational rotations during the coordinated deformation stage within
265 book-house structures were irreversible.

266 **Local fabrics**

267 Consideration of a sub-domain of 12 particles gives insight into local fabric evolution. A typical path of the
268 compact-rebound process is shown in Fig. 6, with evolution from (a) card-house structure \rightarrow (b) book-
269 house structure \rightarrow (c) compacted aggregate \rightarrow (d) post-unloading structure. During the early stage of
270 compaction, a voluminous card-house structure was formed primarily through vertex/edge contacts
271 (Pedrotti and Tarantino 2018) (Fig. 6(a)). This open fabric was rich in interconnected meso-pores due to
272 the relatively large inter-particle distances. As compaction progressed, the inter-particle contacts evolved
273 via the rotation around contact sites and the reduction in inter-particle distances. The card-house structure
274 gradually collapsed, transforming to a book-house structure (Mitchell and Soga 2005) (Fig. 6(b)). Within
275 the parallel-stacked particles (i.e., “books”), micro-pores appeared at the edges owing to the imperfect
276 stacking of monolayered particles (Michot and Villi eras 2006), which has been observed via cryo-electron

277 tomography (Whittaker et al. 2020). Flexible clay particles, characterized by a propensity for tangling
278 (Honorio et al. 2018), contributed to transverse slides and coordinated deformations within “books” in the
279 book-house structure, which is similar to the cake fragment of montmorillonite after high pressure freeze-
280 drying of the suspensions observed by cryo-SEM (Mouzon et al. 2016). This led to further volume reduction
281 with the shrinkage of micro-pores, ultimately forming a compacted aggregate (Fig. 6(c)). After releasing
282 the external pressure, particles rebounded and partial deformations were restored (Fig. 6(d)).

283 **Inter-particle contacts**

284 Evolution of the average contact numbers per particle are depicted as the variation curves with ρ_d in Fig.
285 7. It is the first time to quantitatively explore the changes in arrangements of particle groups via the
286 thorough analyses of inter-particle contact variations during the compact-rebound process. The average
287 number of total contacts per particle CN_{total} showed a stepwise increase during the compact process, as
288 shown in Fig. 7(a). At the formation stage of inter-particle contacts (Stage A), as dispersed clay particles
289 approached each other, many inter-particle contacts were newly formed, leading to an increase in CN_{total}
290 from 2.25 to 2.77. Stage B was dominated by inter-particle contact evolution, along with a small increase
291 in CN_{total} to 3.04. At the stage of coordinated deformations between particles (Stage C), the further
292 reduction in the inter-particle distances led to a continuous increase in CN_{total} to around 4.00. However, the
293 enhanced van der Waals repulsive force (i.e., Pauli repulsion) hindered the further reduction in inter-
294 particle distances, causing a slowdown in contact number growth at the late stage. At Stage D, elastic
295 deformations within particles were recovered and the increasing inter-particle distances directly resulted
296 in the degeneration or loss of inter-particle contacts, with CN_{total} decreasing to about 3.41.

297 The formations and evolutions of inter-particle contacts coexisted in the compact-rebound process, with
298 different dominant forms at each stage, as shown in Fig. 7(b). At Stage A, there was a predominance of
299 newly-formed VV, VF, EE contacts, while at Stage B the evolution from VE and EF contacts to FF contacts
300 was prominent, contributing to a decrease of CN_{VE} and CN_{EF} to about 0.50 and a sustainable increase in
301 CN_{FF} from 0.92 to 1.25. As particles slid transversely and inter-particle distances decreased, Stage C was
302 characterized by the formations of VE, EF and FF contacts, with CN_{VE} , CN_{EF} and CN_{FF} increasing to 0.67, 0.83
303 and 1.69, respectively. After unloading at Stage D, partial EF and FF contacts were detached or gradually
304 degenerated into VV and VF contacts. As a result, CN_{EF} and CN_{FF} decreased to 0.46 and 1.41, respectively.
305 In summary, the stepwise variation stages of inter-particle contacts were alternately characterized by the
306 formation of low-stability contacts and the evolution from low-stability contacts (i.e., VE and EF contacts)
307 to high-stability contacts (i.e., FF contacts) during compaction.

308 **Pore structure**

309 According to the International Union of Pure and Applied Chemistry (IUPAC) (Rouquerol et al. 1994;
310 Kaufhold et al. 2013), pores with diameters of 2–50 nm were categorized as meso-pores (Fig. 6(a)) and
311 pores smaller than 2 nm were categorized as micro-pores (Fig. 6(b)). Cumulative pore size curves and PSD
312 histograms for different dry densities were plotted in Fig. 8. Meso-pores dominated during the formation
313 and collapse of card-house structures ($\rho_d \leq 1.33 \text{ g/cm}^3$), while micro-pores dominated during the
314 coordinated deformation of book-house structures and the rebound process ($\rho_d > 1.33 \text{ g/cm}^3$). Due to the
315 small particle sizes, macro-pores of montmorillonite (50-100 nm) observed via mercury intrusion
316 porosimetry (Souli et al. 2013; Wei et al. 2013) did not emerge in this simulation.

317 The mean pore diameter \bar{D} was defined as the pore diameter smaller than which the pores accounted
318 for 50% of total pores. In the initial model (Fig. 8(a), $\rho_d = 0.50 \text{ g/cm}^3$), meso-pores accounted for about
319 95.2% of the total pore volume. The PSD showed a broad single peak with \bar{D} of around 7.0 nm and a
320 maximum pore diameter of about 12.2 nm. As compaction progressed (Fig. 8(b), $\rho_d = 0.89 \text{ g/cm}^3$), \bar{D}
321 decreased to about 4.4 nm and a minor micro-pore peak gradually generated. The collapse of card-house
322 structures resulted in a unimodal pore size distribution with \bar{D} of about 2.5 nm (Fig. 8(c), $\rho_d = 1.33 \text{ g/cm}^3$).
323 Throughout these stages, pores were mostly interconnected and open (Insets in Fig. 8(a-c)). In the
324 compacted aggregate, micro-pores accounted for 79.2% of the total pore volume. The inter-particle
325 coordinated deformations reduced the sizes of micro-pores, with \bar{D} of the narrow unimodal curve
326 reducing to about 1.2 nm (Fig. 8(d), $\rho_d = 1.98 \text{ g/cm}^3$). Pore spaces became fragmented with discrete and
327 closed pores as deformed particles cleaved through them (Inset in Fig. 8(d)). Unloading caused partial
328 micro-pores to transform into meso-pores, with a reduction of micro-pore proportion to 59.0% (Fig. 8(e),
329 $\rho_d = 1.63 \text{ g/cm}^3$), and pores reconnected as inter-particle distances increased (Inset in Fig. 8(e)). Compared
330 to the brick-like fabric formed by rigid particle models (Honorio et al. 2018; Khabazian et al. 2018), a fabric
331 with low porosity, small open-pores and a higher presence of lenticular pores was reproduced due to the
332 flexible all-atomic clay particle models used in this study.

333 **POTENTIAL ENERGY CONVERSION**

334 **Potential energy density of the whole system**

335 Clearly, a more mechanically stable fabric possessed a lower value of $\Delta\Omega_{\text{sys}}$. As shown in Fig. 9, $\Delta\Omega_{\text{sys}}$
336 decreased to $-1.50 \times 10^{-20} \text{ J/nm}^3$ as the inter-particle contacts gradually evolved into the most stable FF

337 contacts at Stage A and B. However, further compaction at Stage C reduced the inter-particle distances
338 and increased the steric repulsion, resulting in an increase in $\Delta\Omega_{\text{sys}}$ to 4.04×10^{-20} J/nm³. At Stage D with $\rho_d >$
339 1.63 g/cm³, $\Delta\Omega_{\text{sys}}$ decreased to -2.21×10^{-20} J/nm³ due to the recovery of elastic deformations and the
340 enlargement of inter-particle distances. The energy dissipation throughout the entire compact-rebound
341 process was 2.21×10^{-20} J/nm³ greater than the input volume work, and it could be inferred that part of the
342 formation and evolution of inter-particle contacts (Stage A and B) contributed most to the dissipation.
343 Furthermore, $\Delta\Omega_{\text{sys}}$ after rebound was lower than that before unloading at the same dry density, indicating
344 that the remaining irreversible energy dissipation emerged during the coordinated deformations and
345 rebound process.

346 $\Delta\Omega_{\text{in}}$ and $\Delta\Omega_{\text{ia}}$ were of the same order of numerical magnitude, indicating that the influences of the
347 deformations of montmorillonite particles on the potential energy conversion could not be ignored, as
348 shown in Fig. 9. During the compact process, $\Delta\Omega_{\text{in}}$ increased to 2.26×10^{-18} J/nm³ due to the intensified
349 particle deformations, while $\Delta\Omega_{\text{ia}}$ decreased to -2.22×10^{-18} J/nm³ as a result of the evolution of inter-
350 particle contacts. At Stage A and B, where particle deformations were comparatively insignificant,
351 evolution of inter-particle contacts played a major role, and $\Delta\Omega_{\text{ia}}$ was chiefly responsible for the reduction
352 in $\Delta\Omega_{\text{sys}}$. Conversely, particle deformations dominated during Stage C, and the increase in $\Delta\Omega_{\text{in}}$ was the
353 main reason for the rapid increase in $\Delta\Omega_{\text{sys}}$. During Stage D, $\Delta\Omega_{\text{in}}$ decreased by 7.74×10^{-19} J/nm³ due to the
354 recovery of elastic deformations, while $\Delta\Omega_{\text{ia}}$ increased by 7.12×10^{-19} J/nm³ due to the enlargement of inter-
355 particle distances and the degenerations of contacts. Therefore, the reduction in $\Delta\Omega_{\text{in}}$ was the main cause
356 of the decline in $\Delta\Omega_{\text{sys}}$ during the rebound stage. To our knowledge, it is the first time in the literatures to

357 monitor the potential energy conversion during the compaction-rebound process and link it to the fabric
358 evolution observed.

359 Although all particles exhibited similar variation trends in Δu_{in}^{total} and Δu_{ia}^{total} , typical particles No.61 and
360 No.98 were selected for further investigation at particle level in the following two sections, due to their
361 representative deformation characteristics and relatively complete evolution path.

362 **Internal potential energy within a clay particle**

363 Compared to the initial undeformed state, the deformation index K and Δu_{in}^{total} of the typical particle No.98
364 were plotted in Fig. 10. The deformations of particle No.98 during the compact-rebound process could be
365 categorized as five phases in terms of K in Fig. 10(a). At Phase I ($\rho_d \leq 0.69 \text{ g/cm}^3$), the particle was not
366 subjected to significant external forces and experienced minimal deformation ($K < 8.50 \text{ nm}^2$). At Phase II
367 ($0.69 < \rho_d \leq 1.14 \text{ g/cm}^3$), torsional deformation developed and K increased to 190.42 nm^2 . At Phase III (1.14
368 $< \rho_d \leq 1.59 \text{ g/cm}^3$), the particle transformed to a saddle-shape and K sharply increased to 518.67 nm^2 . At
369 Phase IV ($\rho_d > 1.59 \text{ g/cm}^3$), the relaxation of tilting-up vertexes led to a reduction in curvature and the
370 particle's shape transformed to an arch, with K decreasing to 416.17 nm^2 . At Phase V (i.e., the rebound
371 process), partial elastic deformations were released and K gradually decreased to 338.58 nm^2 . The curved
372 platelets in this simulation resemble the montmorillonite clay particles observed via SEM in the previous
373 literatures (Ece et al. 1999; Leong et al. 2022).

374 As mentioned in the *MODEL AND METHOD*, Δu_{in}^{total} consisted of Δu_{in}^{Coul} , Δu_{in}^{vdW} and Δu_{in}^{bonded} . It was found that
375 the repulsive interactions between oxygen atoms contributed most to Δu_{in}^{Coul} during particle deformations,

376 and Δu_{in}^{vdW} raised with the increase of particle volume strain (Supplementary Materials). As shown in Fig.
377 10(b), the contribution of Δu_{in}^{vdW} to Δu_{in}^{total} was less significant than that of Δu_{in}^{Coul} , and Δu_{in}^{bonded} was omitted
378 because it was neglectable compared to Δu_{in}^{Coul} and Δu_{in}^{vdW} .

379 In the compact process, Δu_{in}^{total} increased with dry density and had great relevance to stages of particle
380 deformations. At Phase I, with small deformations, both Δu_{in}^{Coul} and Δu_{in}^{vdW} remained close to zero. At Phase
381 II and III, inter-atomic distances decreased and the redistribution of Na^+ occurred as the particle deformed,
382 as shown in Fig. 10(c), which resulting in the increase of Δu_{in}^{Coul} and Δu_{in}^{vdW} to 3.23×10^{-17} J and 1.10×10^{-17} J,
383 respectively. At Phase IV, Δu_{in}^{vdW} increased to 2.19×10^{-17} J but Δu_{in}^{Coul} kept relatively unchanged, indicating
384 that the increase in Δu_{in}^{total} was attributed to the contribution of Δu_{in}^{vdW} at this phase.

385 In the rebound process (i.e., Phase V), Δu_{in}^{total} decreased from 5.24×10^{-17} J to 4.04×10^{-17} J, among which
386 Δu_{in}^{vdW} decreased by 1.70×10^{-17} J while Δu_{in}^{Coul} increased by 0.52×10^{-17} J, suggesting the reduction of Δu_{in}^{total} in
387 the rebound process chiefly resulted from the decrease of van der Waals repulsion as partial elastic
388 deformations recovered and volume strain decreased. However, Δu_{in}^{vdW} became greater and Δu_{in}^{Coul} became
389 smaller than those before rebound with identical dry density, which indicated irreversible changes in van
390 der Waals and Coulombic electrostatic interactions emerged during the rebound process, due to plastic
391 deformations (such as, atomic dislocations and ruptures) and the non-recoverability of Na^+ redistribution.

392 **Interaction potential energy between clay particles**

393 Δu_{ia}^{total} , Δu_{ia}^{Coul} and Δu_{ia}^{vdW} between the typical particles No.61 and No.98 are plotted in Fig. 11. In the
394 compaction process, Δu_{ia}^{total} decreased with dry density in stages. Obviously, Δu_{ia}^{total} reached a plateau once

395 a specific inter-particle contact (i.e., VE, EF and FF contacts) was formed. Δu_{ia}^{total} decreased by 0.28×10^{-18} J
396 as particles evolved from VE contact into EF contact, and decreased by 9.12×10^{-18} J as they evolved from
397 EF contact into FF contact. It could be inferred that Δu_{ia}^{total} decreased with the enlargement of contact areas.
398 Calculations of interaction force between particles (Supplementary Materials) indicated that the attractive
399 electrostatic force of cations on negatively-charged clay crystalline layer slightly exceeded the summation
400 of repulsive electrostatic forces between clay crystalline layers and between cations, while the van der
401 Waals force between atoms at the contact sites was repulsive and that between atoms far from contact
402 sites was attractive. As the particle rotated around the contact sites, positive work was done by
403 electrostatic attraction and the van der Waals attraction between atoms far from the contact sites, while
404 the van der Waals repulsion at the contact sites almost did no work due to the constant contact distances,
405 leading to the decreases of Δu_{ia}^{Coul} and Δu_{ia}^{vdW} as the inter-particle contacts evolved. This is similar to the
406 detachment mechanism in the concept model proposed by Pedrotti (Pedrotti and Tarantino 2018),
407 resulting in an irreversible volume change.

408 A hysteresis loop of Δu_{ia}^{total} was observed throughout the compaction and rebound process. Under identical
409 dry density, there was a slight change in Δu_{ia}^{vdW} before and after rebound, indicating that it was almost
410 reversible. However, there was a significant difference in Δu_{ia}^{Coul} before and after rebound, highlighting that
411 the irreversibility of electrostatic interaction was attributed to the hysteresis observed in the variation
412 curve of Δu_{ia}^{total} .

413 CONCLUSIONS

414 This paper proposes an all-atomic molecular dynamic modelling framework to investigate the compact-

415 rebound process of anhydrous montmorillonite platelets from the view of fabric evolution and potential
416 energy conversion. The fabric evolution, which was characterized by card-house structure, book-house
417 structure, compacted aggregate and post-unloading structure, was quantified via orientation order
418 parameter, variations in inter-particle contacts, pore size distribution and pore space tomography.
419 Potential energy density calculations were performed to analyze the laws of energy conversion and
420 dissipation in clays. The variations of the internal potential energy and interaction potential energy of
421 typical particles were investigated in terms of electrostatic and van der Waals terms for different stages in
422 the compact-rebound process.

423 Compared to the brick-like fabric formed by rigid particle models, a fabric with smaller open pores and
424 more lenticular pores was reproduced with flexible clay particle models in this study. The average number
425 of total contacts per particle increased stepwise in the compact process and decreased in the rebound
426 process. Generation of low-stability contacts (e.g., VV, VF and EE) dominated during the formation of card-
427 house structures. During the collapse of card-house structures into book-house structures, the fabric was
428 dominated by the evolution from low-stability contacts to high-stability contacts (e.g., EF and FF). Partial
429 contacts formed at the later coordinated deformation stage were lost or degenerated during rebound.

430 The variations in total potential energy density included the internal potential energy density and
431 interaction potential energy density, which were of the same order of magnitudes in the compact-rebound
432 process. The internal term increased during compaction and decreased during rebound, while the
433 interaction term showed the opposite trend. The total potential energy density decreased when inter-
434 particle contacts evolved to more stable types, which mainly resulted from a significant reduction in

435 interaction potential energy density between particles. Afterwards, it raised dramatically during the stage
436 of coordinated deformations and gradually decreased during rebound, primarily owing to the
437 corresponding variations in the internal potential energy within particles.

438 The deformation of a clay particle and its induced variations in the internal potential energy within the
439 particle during the compact-rebound process could be simulated with the flexible clay particle model. The
440 internal potential energy of a typical particle increased during compaction but decreased during rebound.

441 The electrostatic term consistently contributed more to the internal potential energy within the particle
442 than the van der Waals term, but the latter played an indispensable role as particle deformations became
443 relatively large in the later compact and rebound stages. The interaction potential energy between
444 particles remained unchanged once a specific contact type was formed, while it decreased stepwise
445 primarily due to the electrostatic interaction when the inter-particle contact evolved into a more stable
446 type and the contact area enlarged. The hysteresis of the total interaction potential energy observed in
447 the compact-rebound process was mainly attribute to the irreversibility of the electrostatic interaction.

448 Computational expense for such models was significant. The simulation presented in this study took nearly
449 6 months of consecutive calculations on high-performance computer clusters. The size of particles was
450 small (about 1/10 of the transverse size of actual montmorillonite particles) and monotypic, which
451 resulted in large values of energy density, fictitious high stiffness of clay (Ebrahimi et al. 2016b) and
452 intensive thermodynamic fluctuations with respect to those obtained in the laboratory tests. There was a
453 lack in considering the influences water molecules, which could hydrate surface cations to form the
454 electrical double layers, in turns changing the inter-particle interactions. In future work, better simulations

455 of compaction and other macroscopic behaviors of clays via all-atomic MD can be achieved with
456 consideration of a greater number of larger hydrated clay particles as computational capacity develops.

457

458 **NOTATION**

459 CN average number of contacts per particle (subscripts stand for specific contact types)

460 D pore diameter

461 \bar{D} mean pore diameter (i.e., pores smaller than this size account for 50% of the total pores)

462 e void ratio (e_0 is the void ratio of initial model before compaction)

463 K deformation index of the particle

464 \mathbf{n} normal vector of particle surfaces

465 N total number of octahedral metal atoms in each particle

466 N_p total number of clay particles in the simulation box

467 S_z orientation order parameter of particles with respect to the z-axis

468 u_{ia}^{Coul} Coulombic electrostatic term of interaction potential energy between two clay particles

469 u_{ia}^{vdW} van der Waals term of interaction potential energy between two clay particles

470 u_{ia}^{total} total interaction potential energy between two clay particles

471 u_{in}^{bonded} bonded term of internal potential energy within a single clay particle

472 u_{in}^{Coul} Coulombic electrostatic term of internal potential energy within a single clay particle

473 u_{in}^{vdW} van der Waals term of internal potential energy within a single clay particle

474 u_{in}^{total} total internal potential energy within a single clay particle

475	U^{angle}	the angle-bending potential energy of the whole system
476	U^{bond}	the bond-stretching potential energy of the whole system
477	U^{bonded}	the bonded potential energy of the whole system
478	U^{Coul}	the Coulomb electrostatic potential energy of the whole system
479	U^{vdW}	the van der Waals potential energy of the whole system
480	$U^{\text{non-bonded}}$	the non-bonded potential energy of the whole system
481	U^{total}	the total potential energy of the whole system (U_0^{total} is the initial total potential energy)
482	V	volume of clay (V_0 is the volume of the initial model before compaction)
483	δ_z	z-deflection of the deformed particle
484	ρ_d	dry density (ρ_{d0} is the dry density of initial model before compaction)
485	Ω_{ia}	interaction potential energy density of the whole system
486	Ω_{in}	internal potential energy density of the whole system
487	Ω_{sys}	total potential energy density of the whole system

488

489 **DATA AVAILABILITY STATEMENT**

490 All data, models, and code generated or used during the study appear in the submitted article.

491

492 **ACKNOWLEDGEMENTS**

493 The financial supports received from the National Natural Science Foundation of China (NSFC, Grant No.

494 51988101 and 42077241) are gratefully acknowledged. Hang-Jun Wu in the Centre of Cryo-Electron
495 Microscopy (CCEM), Zhejiang University is greatly appreciated for his technical assistance.

496

497 **SUPPLEMENTAL MATERIALS**

498 Figs. S1–S12 and Tables S1-S4 are available online in the ASCE Library (www.ascelibrary.org). The video of
499 the whole compress-rebound process can also be found online in the ASCE Library (www.ascelibrary.org).

500

501 **REFERENCES**

502 Ahmed, H. R., and Abduljawwad, S. N. 2017. "Nano-Level Constitutive Model for Expansive Clays."
503 *Géotechnique*, 67(3), 187-207. <https://doi.org/10.1680/jgeot.15.P.140>.

504 Allen, M. P., and Tildesley, D. J. 2017. *Computer Simulation of Liquids*, Oxford University Press, Oxford,
505 United Kingdom.

506 Aminpour, P., and Sjoblom, K. J. 2019. "Multi-Scale Modelling of Kaolinite Triaxial Behaviour." *Geotech.*
507 *Lett.*, 9(3), 178-185. <https://doi.org/10.1680/jgele.18.00194>.

508 Anandarajah, A., and Lu, N. 1991. "Numerical Study of the Electrical Double - Layer Repulsion between
509 Non - Parallel Clay Particles of Finite Length." *Int. J. Numer. Anal. Methods Geomech.*, 15(10), 683-703
510 <https://doi.org/10.1002/nag.1610151002>.

511 Anandarajah, A. 1994. "Discrete - Element Method for Simulating Behavior of Cohesive Soil." *J. Geotech.*
512 *Eng.*, 120(9), 1593-1613. [https://doi.org/10.1061/\(ASCE\)0733-9410\(1994\)120:9\(1593\)](https://doi.org/10.1061/(ASCE)0733-9410(1994)120:9(1593)).

513 Anandarajah, A., and Chen, J. 1995. "Single Correction Function for Computing Retarded van der Waals
514 Attraction." *J. Colloid Interface Sci.*, 176(2), 293–300. <https://doi.org/10.1006/jcis.1995.9964>.

515 Anoukou, K., Zaoui, A., Zaïri, F., Naït-Abdelaziz, M., and Gloaguen, J. M. 2015. "Structural and
516 thermodynamics properties of organo-modified montmorillonite clay." *Physica E: Low-dimensional*
517 *Systems and Nanostructures*, 65, 56-60. <https://doi.org/10.1016/j.physe.2014.07.025>.

518 Arun, K. S., Huang, T. S., and Blostein, S. D. 1987. "Least-Squares Fitting of Two 3-D Point Sets." *IEEE Trans.*
519 *Pattern Anal. Mach. Intell.*, PAMI-9(5), 698-700. <https://doi.org/10.1109/TPAMI.1987.4767965>.

520 Bandera, S., O'Sullivan, C., Tangney, P., and Angioletti-Uberti, S. 2021. "Coarse-Grained Molecular
521 Dynamics Simulations of Clay Compression." *Comput. Geotech.*, 138, 104333-104350.
522 <https://doi.org/10.1016/j.compgeo.2021.104333>.

523 Bayesteh, H., and Mirghasemi, A. A. 2013. "Numerical Simulation of Pore Fluid Characteristic Effect on the
524 Volume Change Behavior of Montmorillonite Clays." *Comput. Geotech.*, 48, 146-155.
525 <https://doi.org/10.1016/j.compgeo.2012.10.007>.

526 Benhamida, A., Djeran-Maigre, I., Dumontet, H., and Smaoui, S. 2005. "Clay compaction modelling by
527 homogenization theory." *Int. J. Rock Mech. Min. Sci.*, 42(7-8), 996-1005.
528 <https://doi.org/10.1016/j.ijrmms.2005.05.021>.

529 Bhattacharya, S., and Gubbins, K. E. 2006. "Fast Method for Computing Pore Size Distributions of Model
530 Materials." *Langmuir*, 22(18), 7726-7731. <https://doi.org/10.1021/la052651k>.

531 Carrier, B., Vandamme, M., Pellenq, R. J., Bornert, M., Ferrage, E., Hubert, F., and Van Damme, H. 2016.
532 "Effect of Water on Elastic and Creep Properties of Self-Standing Clay Films." *Langmuir*, 32(5), 1370-1379.
533 <https://doi.org/10.1021/acs.langmuir.5b03431>.

534 Chen, J., and Anandarajah, A. 1996. "Van der Waals Attraction between Spherical Particles." *J. Colloid*
535 *Interface Sci.*, 180(2), 519–523. <https://doi.org/10.1006/jcis.1996.0332>.

536 Cheng, Z., and Wang, J. 2018. "A Particle-Tracking Method for Experimental Investigation of Kinematics of
537 Sand Particles under Triaxial Compression." *Powder Technol.*, 328, 436-451.
538 <https://doi.org/10.1016/j.powtec.2017.12.071>.

539 Cundall, P. A., and Strack, O. D. L. 1979. "A discrete numerical model for granular assemblies."
540 *Géotechnique*, 29(1), 47-65. <https://doi.org/10.1680/geot.1979.29.1.47>.

541 Cygan, R. T., Liang, J.-J., and Kalinichev, A. G. 2004. "Molecular Models of Hydroxide, Oxyhydroxide, and Clay
542 Phases and the Development of a General Force Field." *J. Phys. Chem. B*, 108(4), 1255-1266.
543 <https://doi.org/10.1021/jp0363287>.

544 Cygan, R. T., Greathouse, J. A., and Kalinichev, A. G. 2021. "Advances in Clayff Molecular Simulation of
545 Layered and Nanoporous Materials and Their Aqueous Interfaces." *J. Phys. Chem. C*, 125(32), 17573-17589.
546 <https://doi.org/10.1021/acs.jpcc.1c04600>.

547 de Bono, J., and McDowell, G. 2023a. "Simulating multifaceted interactions between kaolinite platelets."
548 *Powder Technol.*, 413. <https://doi.org/10.1016/j.powtec.2022.118062>.

549 de Bono, J., and McDowell, G. 2023b. "Particle-scale simulations of the compression and shearing of kaolin
550 clay." *Geotechnique*. <https://doi.org/10.1680/jgeot.22.00423>.

551 Ebrahimi, D. 2014. "Multiscale Modeling of Clay Water Systems." Doctor of Philosophy PhD thesis,
552 Massachusetts Institute of Technology, Cambridge, USA.

553 Ebrahimi, D., Whittle, A. J., and Pellenq, R. J. M. 2014. "Mesoscale Properties of Clay Aggregates from
554 Potential of Mean Force Representation of Interactions between Nanoplatelets." *J. Chem. Phys.*, 140(15),
555 154309. <https://doi.org/10.1063/1.4870932>.

556 Ebrahimi, D., Pellenq, R. J. M., and Whittle, A. J. 2016a. "Mesoscale Simulation of Clay Aggregate Formation
557 and Mechanical Properties." *Granul. Matter*, 18(3), 49. <https://doi.org/10.1007/s10035-016-0655-8>.

558 Ebrahimi, D., Whittle, A. J., and Pellenq, R. J. M. 2016b. "Effect of Polydispersity of Clay Platelets on the
559 Aggregation And Mechanical Properties of Clay at the Mesoscale." *Clays Clay Miner.*, 64(4), 425-437.
560 <https://doi.org/10.1346/ccmn.2016.0640407>.

561 Ece, Ö. I., Çoban, F. z., Güngör, N., and Suner, F. 1999. "Clay Mineralogy and Occurrence of Ferrian Smectites
562 between Serpentinite Saproplites and Basalts in Biga Peninsula, Northwest Turkey." *Clays Clay Miner.*, 47(3),
563 241-251. <https://doi.org/10.1346/ccmn.1999.0470301>.

564 Everaers, R., and Ejtehadi, M. R. 2003. "Interaction potentials for soft and hard ellipsoids." *Phys Rev E Stat*

565 *Nonlin Soft Matter Phys*, 67, 041710. <https://doi.org/10.1103/PhysRevE.67.041710>.

566 Frankel, D., and Smit, B. 2002. *Understanding Molecular Simulation: From Algorithms to Applications*,
567 Academic Press, Bodmin, Cornwall, Great Britain.

568 Gay, J. G., and Berne, B. J. 1981. "Modification of the overlap potential to mimic a linear site–site
569 potential." *The Journal of Chemical Physics*, 74(6), 3316-3319. <https://doi.org/10.1063/1.441483>.

570 Gu, X., Hu, J., and Huang, M. 2015. " K_0 of Granular Soils: A Particulate Approach." *Granul. Matter*, 17(6),
571 703-715. <https://doi.org/10.1007/s10035-015-0588-7>.

572 Guo, Y., and Yu, X. 2017. "Characterizing the surface charge of clay minerals with Atomic Force Microscope
573 (AFM)." *AIMS Mater. Sci.*, 4(3), 582-593. <https://doi.org/10.3934/matersci.2017.3.582>.

574 Guo, Y., and Yu, X. 2019. "A holistic computational model for prediction of clay suspension structure."
575 *International Journal of Sediment Research*, 34(4), 345-354. <https://doi.org/10.1016/j.ijsrc.2018.12.002>.

576 Ho, T. A., Greathouse, J. A., Wang, Y., and Criscenti, L. J. 2017. "Atomistic Structure of Mineral Nano-
577 aggregates from Simulated Compaction and Dewatering." *Sci. Rep.*, 7(1), 15286.
578 <https://doi.org/10.1038/s41598-017-15639-4>.

579 Hockney, R. W., and Eastwood, J. W. 1989. *Computer Simulation using Particles*, Adam Hilger.

580 Honorio, T., Brochard, L., Vandamme, M., and Lebee, A. 2018. "Flexibility of Nanolayers and Stacks:
581 Implications in the Nanostructuration of Clays." *Soft Matter*, 14(36), 7354-7367.

582 <https://doi.org/10.1039/c8sm01359d>.

583 Humphrey, W., Dalke, A., and Schulten, K. 1996. "VMD: Visual Molecular Dynamics." *J. Mol. Graph.*, 14,
584 33-38. [https://doi.org/10.1016/0263-7855\(96\)00018-5](https://doi.org/10.1016/0263-7855(96)00018-5).

585 Imseeh, W. H., Druckrey, A. M., and Alshibli, K. A. 2018. "3D Experimental Quantification of Fabric and
586 Fabric Evolution of Sheared Granular Materials using Synchrotron Micro-Computed Tomography." *Granul.*
587 *Matter*, 20(2), 24. <https://doi.org/10.1007/s10035-018-0798-x>.

588 Jaradat, K. A., and Abdelaziz, S. L. 2019. "On the use of discrete element method for multi-scale assessment
589 of clay behavior." *Comput. Geotech.*, 112, 329-341. <https://doi.org/10.1016/j.compgeo.2019.05.001>.

590 Jaradat, K. A., and Abdelaziz, S. L. 2023. "Simplifying the physico-chemical contacts in cohesive soils for
591 efficient DEM simulations." *Comput. Geotech.*, 154. <https://doi.org/10.1016/j.compgeo.2022.105155>.

592 Jiang, M. J. 2019. "New Paradigm for Modern Soil Mechanics: Geomechanics from Micro to Macro." *Chin.*
593 *J. Geotech.*, 41(2), 195-254. <https://doi.org/10.11779/CJGE201902001>.

594 Kang, X., Sun, H.-m., Yang, W., and Chen, R.-p. 2020. "Wettability of clay aggregates—A coarse-grained
595 molecular dynamic study." *Appl. Surf. Sci.*, 532. <https://doi.org/10.1016/j.apsusc.2020.147423>.

596 Kaufhold, S., Plötze, M., Klinkenberg, M., and Dohrmann, R. 2013. "Density and Porosity of Bentonites." *J.*
597 *Porous Mater.*, 20(1), 191-208. <https://doi.org/10.1007/s10934-012-9589-7>.

598 Khabazian, M., Mirghasemi, A. A., and Bayesteh, H. 2018. "Compressibility of Montmorillonite/Kaolinite

599 Mixtures in Consolidation Testing using Discrete Element Method." *Comput. Geotech.*, 104, 271-280.
600 <https://doi.org/10.1016/j.compgeo.2018.09.005>.

601 Lavikainen, L. P., Hirvi, J. T., Kasa, S., Schatz, T., and Pakkanen, T. A. 2015. "Stability of Dioctahedral 2:1
602 Phyllosilicate Edge Structures based on Pyrophyllite Models." *Theor. Chem. Acc.*, 134(9), 112.
603 <https://doi.org/10.1007/s00214-015-1715-6>.

604 Leong, Y.-K., Liu, P., Au, P.-I., Clode, P., and Liu, J. 2022. "Microstructure and Time-Dependent Behavior of
605 STx-1b Calcium Montmorillonite Suspensions." *Clays Clay Miner.*, 69(6), 787-796.
606 <https://doi.org/10.1007/s42860-021-00170-5>.

607 Lowenstein, W. 1954. "The Distribution of Aluminum in the Tetrahedra of Silicates and Aluminates." *Am.*
608 *Mineral.*, 39(1-2), 92-96

609 Lu, N., and Anandarajah, A. 1992. "Empirical Estimation of Double - Layer Repulsive Force between Two
610 Inclined Clay Particles of Finite Length." *J. Geotech. Eng.*, 118(4), 628-634.
611 [https://doi.org/10.1061/\(ASCE\)0733-9410\(1992\)118:4\(628\)](https://doi.org/10.1061/(ASCE)0733-9410(1992)118:4(628)).

612 Lu, T., and Chen, F. 2012. "Multiwfn: A Multifunctional Wavefunction Analyzer." *J. Comput. Chem.*, 33(5),
613 580-592. <https://doi.org/10.1002/jcc.22885>.

614 Martins, D. M. S., Molinari, M., Gonçalves, M. A., Mirão, J. P., and Parker, S. C. 2014. "Toward Modeling
615 Clay Mineral Nanoparticles: The Edge Surfaces of Pyrophyllite and Their Interaction with Water." *J. Phys.*
616 *Chem. C*, 118(47), 27308-27317. <https://doi.org/10.1021/jp5070853>.

617 Mazo, M. A., Manevitch, L. I., Gusarova, E. B., Shamaev, M. Y., Berlin, A. A., Balabaev, N. K., and Rutledge,
618 G. C. 2008. "Molecular Dynamics Simulation of Thermomechanical Properties of Montmorillonite Crystal.
619 1. Isolated Clay Nanoplate." *J. Phys. Chem. B*, 112, 2964-2969. <https://doi.org/10.1021/jp076022q>.

620 Michot, L. J., and Villiéras, F. 2006. "Surface Area and Porosity." *Handbook of Clay Science*, F. Bergaya, B. K.
621 G. Theng, and G. Lagaly, eds., 965-978.

622 Mitchell, J. K., and Soga, K. 2005. *Fundamentals of Soil Behavior*, John Wiley & Sons, Inc., Hoboken, New
623 Jersey.

624 Mouzon, J., Bhuiyan, I. U., and Hedlund, J. 2016. "The Structure of Montmorillonite Gels Revealed by
625 Sequential Cryo-XHR-SEM Imaging." *J. Colloid Interface Sci.*, 465, 58-66.
626 <https://doi.org/10.1016/j.jcis.2015.11.031>.

627 Nie, J.-Y., Cao, Z.-J., Li, D.-Q., and Cui, Y.-F. 2021. "3D DEM Insights into the Effect of Particle Overall
628 Regularity on Macro and Micro Mechanical Behaviours of Dense Sands." *Comput. Geotech.*, 132, 103965.
629 <https://doi.org/10.1016/j.compgeo.2020.103965>.

630 O'Sullivan, C. 2011. *Particulate Discrete Element Modelling: A Geomechanics Perspective*, Spron Press,
631 Abingdon, UK.

632 Pagano, A. G., Magnanimo, V., Weinhart, T., and Tarantino, A. 2020. "Exploring the micromechanics of non-
633 active clays by way of virtual DEM experiments." *Géotechnique*, 70(4), 303-316.
634 <https://doi.org/10.1680/jgeot.18.P.060>.

635 Pedrotti, M., and Tarantino, A. 2018. "An Experimental Investigation into the Micromechanics of Non-
636 Active Clays." *Géotechnique*, 68(8), 666-683. <https://doi.org/10.1680/jgeot.16.P.245>.

637 Pouvreau, M., Greathouse, J. A., Cygan, R. T., and Kalinichev, A. G. 2017. "Structure of Hydrated Gibbsite
638 and Brucite Edge Surfaces: DFT Results and Further Development of the ClayFF Classical Force Field with
639 Metal–O–H Angle Bending Terms." *J. Phys. Chem. C*, 121(27), 14757-14771.
640 <https://doi.org/10.1021/acs.jpcc.7b05362>.

641 Pouvreau, M., Greathouse, J. A., Cygan, R. T., and Kalinichev, A. G. 2019. "Structure of Hydrated Kaolinite
642 Edge Surfaces: DFT Results and Further Development of the ClayFF Classical Force Field with Metal–O–H
643 Angle Bending Terms." *J. Phys. Chem. C*, 123(18), 11628-11638. <https://doi.org/10.1021/acs.jpcc.9b00514>.

644 Prishchenko, D. A., Zenkov, E. V., Mazurenko, V. V., Fakhruilin, R. F., Lvov, Y. M., and Mazurenko, V. G. 2018.
645 "Molecular dynamics of the halloysite nanotubes." *Phys Chem Chem Phys*, 20(8), 5841-5849.
646 <https://doi.org/10.1039/c7cp06575b>.

647 Quirk, J. P., and Aylmore, L. A. G. 1971. "Domains and Quasi-Crystalline Regions in Clay Systems." *Soil Sci.*
648 *Soc. Am. J.*, 35(4), 652-654. <https://doi.org/10.2136/sssaj1971.03615995003500040046x>.

649 Rouquerol, J., Avnir, D., Fairbridge, C. W., Everett, D. H., Haynes, J. H., Pernicone, N., Ramsay, J. D. F., Sing,
650 K. S. W., and Unger, K. K. 1994. "Recommendations for Characterisation of Porous Solids (Technical
651 Report)." *Pure Appl. Chem.*, 66(8), 1739-1758. <https://doi.org/10.1351/pac199466081739>.

652 Santagata, M., Bobet, A., Howayek, A. E., Ochoa, F., Sinfield, J. V., and Johnston, C. T. 2014. "Building a

653 Nanostructure in the Pore Fluid of Granular Soils." In *Proc., Geomechanics from Micro to Macro*, 1377-
654 1382. London, UK: Taylor & Francis Group.

655 Santamarina, J. C. 2003. "Soil Behavior at the Microscale: Particle Forces." In *Proc., Symposium on Soil*
656 *Behavior and Soft Ground Construction Honoring Charles C. Ladd*, 25-56. USA: American Society of Civil
657 Engineers.

658 Schaettle, K., Ruiz Pestana, L., Head-Gordon, T., and Lammers, L. N. 2018. "A structural coarse-grained
659 model for clays using simple iterative Boltzmann inversion." *J. Chem. Phys.*, 148(22), 222809.
660 <https://doi.org/10.1063/1.5011817>.

661 Sjoblom, K. J. 2016. "Coarse-Grained Molecular Dynamics Approach to Simulating Clay Behavior." *J.*
662 *Geotech. Geoenviron. Eng.*, 142(2), 06015013. [https://doi.org/10.1061/\(asce\)gt.1943-5606.0001394](https://doi.org/10.1061/(asce)gt.1943-5606.0001394).

663 Skipper, N. T., Chang, F.-R. C., and Sposito, G. 1995. "Monte Carlo Simulation of Interlayer Molecular
664 Structure in Swelling Clay Minerals.1. Methodology." *Clays Clay Miner.*, 43(3), 285-293.
665 <https://doi.org/10.1346/CCMN.1995.0430303>.

666 Souli, H., Fleureau, J. M., Trabelsi-Ayadi, M., and Taibi, S. 2013. "A multi-scale study of the effect of zinc
667 and lead on the hydromechanical behaviour and fabric of a montmorillonite." *Géotechnique*, 63(10), 880-
668 884. <https://doi.org/10.1680/geot.13.P.016>.

669 Sperry, J. M., and Peirce, J. J. 1999. "Ion exchange and surface charge on montmorillonite clay." *Water*
670 *Environment Research*, 71(3), 316-322. <https://doi.org/10.2307/25045217>.

671 Suter, J. L., Anderson, R. L., Christopher Greenwell, H., and Coveney, P. V. 2009. "Recent Advances in Large-
672 Scale Atomistic and Coarse-Grained Molecular Dynamics Simulation of Clay Minerals." *J. Mater. Chem.*,
673 19(17), 2482-2493. <https://doi.org/10.1039/b820445d>.

674 Tarantino, A., and De Col, E. 2008. "Compaction behaviour of clay." *Géotechnique*, 58(3), 199-213.
675 <https://doi.org/10.1680/geot.2008.58.3.199>.

676 Thompson, A. P., Aktulga, H. M., Berger, R., Bolintineanu, D. S., Brown, W. M., Crozier, P. S., in 't Veld, P. J.,
677 Kohlmeyer, A., Moore, S. G., Nguyen, T. D., Shan, R., Stevens, M. J., Tranchida, J., Trott, C., and Plimpton, S.
678 J. 2022. "LAMMPS - A Flexible Simulation Tool for Particle-based Materials Modeling at the Atomic, Meso,
679 and Continuum Scales." *Comput. Phys. Commun.*, 271, 108171-108204.
680 <https://doi.org/10.1016/j.cpc.2021.108171>.

681 Underwood, T. R., and Bourg, I. C. 2020. "Large-Scale Molecular Dynamics Simulation of the Dehydration
682 of a Suspension of Smectite Clay Nanoparticles." *J. Phys. Chem. C*, 124(6), 3702-3714.
683 <https://doi.org/10.1021/acs.jpcc.9b11197>.

684 van Olphen, H. 1977. *An Introduction to Clay Colloid Chemistry: For Clay Technologists, Geologists and Soil*
685 *Scientists*, Wiley, New York.

686 Vijayan, A., Gan, Y., and Annabattula, R. K. 2020. "Evolution of Fabric in Spherical Granular Assemblies
687 under the Influence of Various Loading Conditions through DEM." *Granul. Matter*, 22(2), 34.
688 <https://doi.org/10.1007/s10035-020-1000-9>.

689 Wang, X., Ramirez-Hinestrosa, S., Dobnikar, J., and Frenkel, D. 2020. "The Lennard-Jones potential: when
690 (not) to use it." *Phys. Chem. Chem. Phys.*, 22(19), 10624-10633. <https://doi.org/10.1039/c9cp05445f>.

691 Wei, X., Hattab, M., Fleureau, J.-M., and Hu, R. 2013. "Micro–macro-experimental study of two clayey
692 materials on drying paths." *Bull. Eng. Geol. Environ.*, 72(3-4), 495-508. [https://doi.org/10.1007/s10064-](https://doi.org/10.1007/s10064-013-0513-4)
693 013-0513-4.

694 White, G. N., and Zelazny, L. W. 1988. "Analysis and Implications of the Edge Structure of Dioctahedra
695 Phyllosilicates." *Clays Clay Miner.*, 36, 141-146. <https://doi.org/10.1346/CCMN.1988.0360207>.

696 Whittaker, M. L., Comolli, L. R., Gilbert, B., and Banfield, J. F. 2020. "Layer size polydispersity in hydrated
697 montmorillonite creates multiscale porosity networks." *Appl. Clay Sci.*, 190.
698 <https://doi.org/10.1016/j.clay.2020.105548>.

699 Xiong, W., Wang, J., and Wu, M. 2022. "Effects of Morphological Gene Decay and Mutation on the Micro–
700 Macro Mechanical Behaviours of Granular Soils." *Géotechnique*, 1-19.
701 <https://doi.org/10.1680/jgeot.21.00180>.

702 Yao, M. 2002. "Three-Dimensional Discrete Element Method Analysis of Cohesive Soil." Doctor of
703 Philosophy, The John Hopkins University, Baltimore, Maryland.

704 Yin, Z., Wang, P., and Dai, S. 2023. "Microstructures and Micromechanics of Geomaterials." *J. Zhejiang*
705 *Univ.-Sc. A*, 24(4), 299-302. <https://doi.org/10.1631/jzus.A2300MMG>.

706 Zhao, B., Wang, J., Coop, M. R., Viggiani, G., and Jiang, M. 2015. "An Investigation of Single Sand Particle

707 Fracture using X-Ray Micro-Tomography." *Géotechnique* 65(8), 625-641.

708 <https://doi.org/10.1680/geot.4.P.157>.

709 Zhao, J., and Guo, N. 2013. "Unique Critical State Characteristics in Granular Media Considering Fabric

710 Anisotropy." *Géotechnique*, 63(8), 695-704. <https://doi.org/10.1680/geot.12.P.040>.

711 Zhu, H., Whittle, A. J., Pellenq, R. J. M., and Ioannidou, K. 2019. "Mesoscale Simulation of Aggregation of

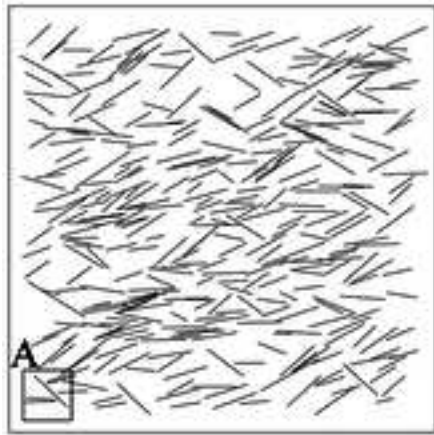
712 Imogolite Nanotubes from Potential of Mean Force Interactions." *Mol. Phys.*, 117(22), 3445-3455.

713 <https://doi.org/10.1080/00268976.2019.1660817>.

714 Zhu, L., Shen, W., Shao, J., and He, M. 2021. "Insight of molecular simulation to better assess deformation

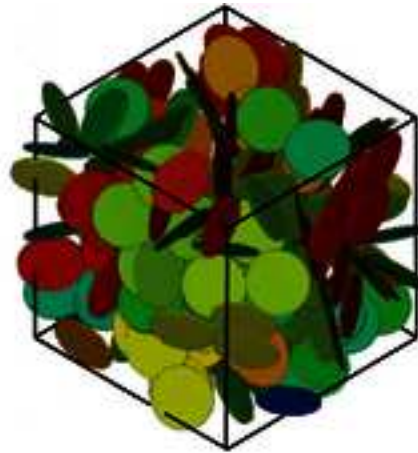
715 and failure of clay-rich rocks in compression and extension." *Int. J. Rock Mech. Min. Sci.*, 138.

716 <https://doi.org/10.1016/j.ijrmms.2020.104589>.



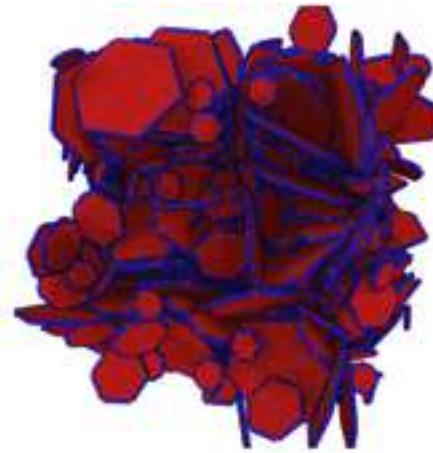
(a) 2D-line discrete element model

Adapted from H. Bayesteh and A. A. Mirghasemi (2013). Copyright 2012 Elsevier Ltd.



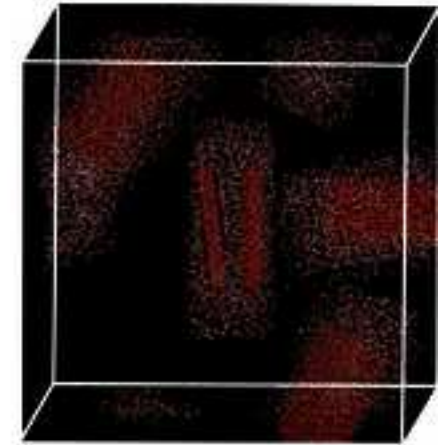
(b) Ellipsoidal particle model

Adapted from D. Ebrahimi et al. (2014). Copyright 2014 AIP Publishing LLC.



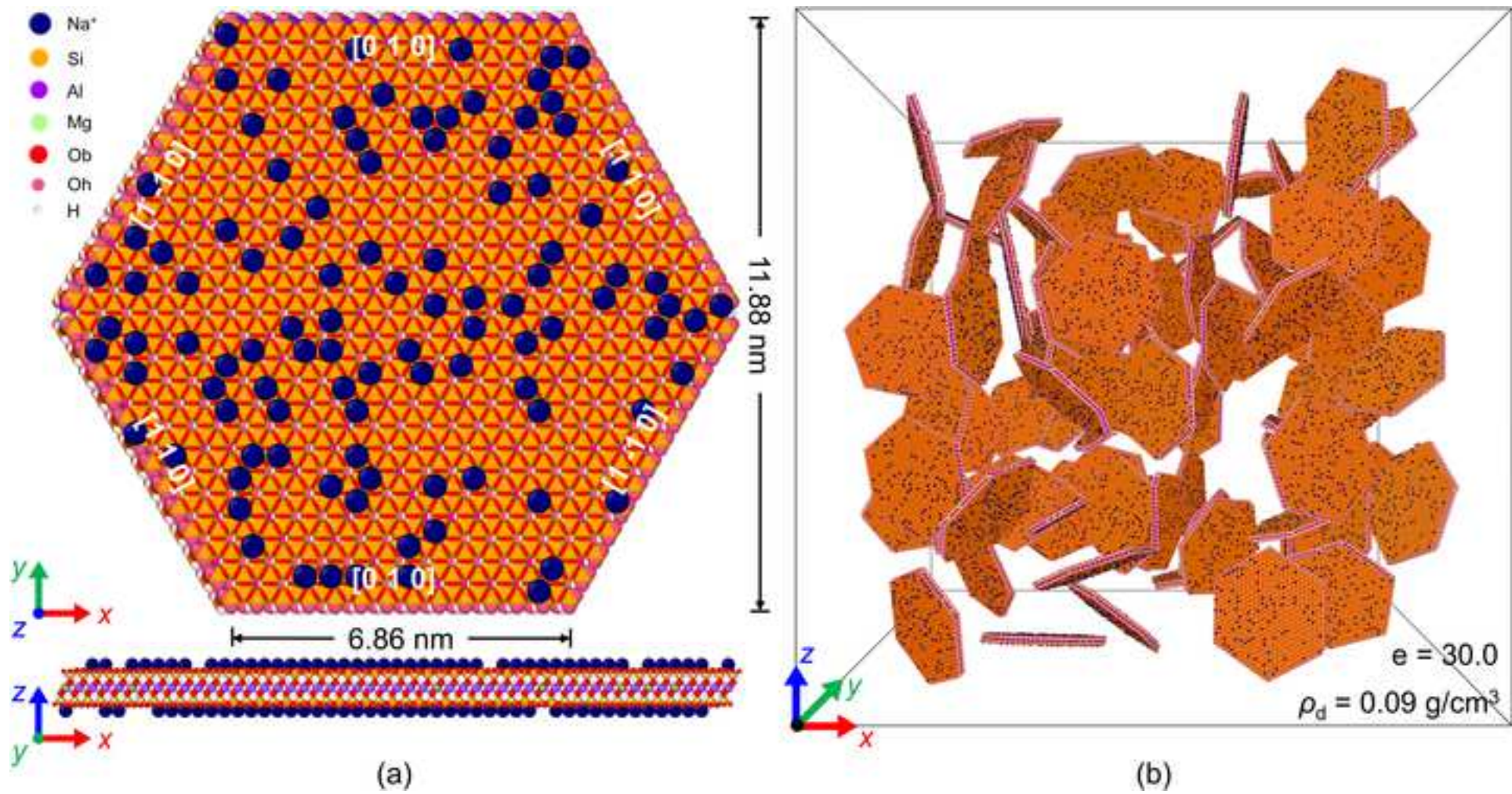
(c) United-bead particle model


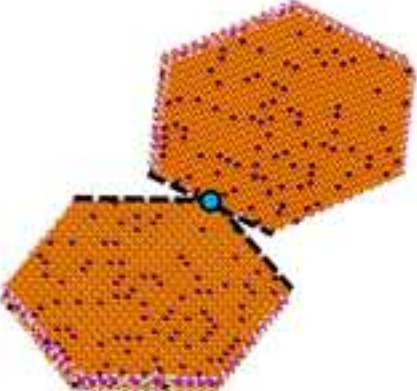

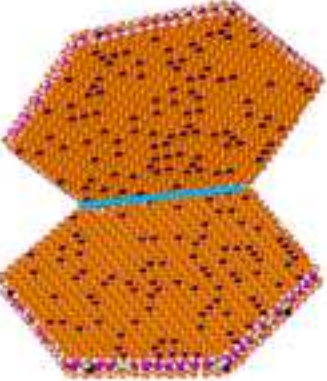
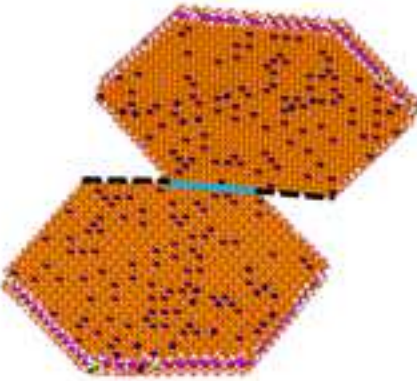
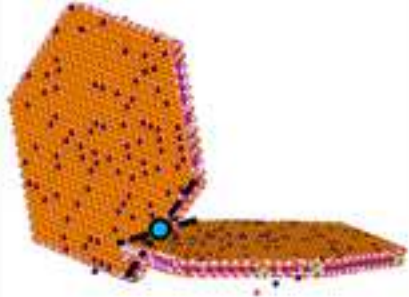

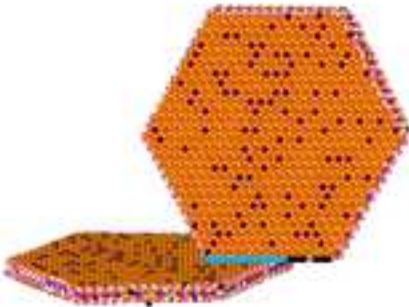
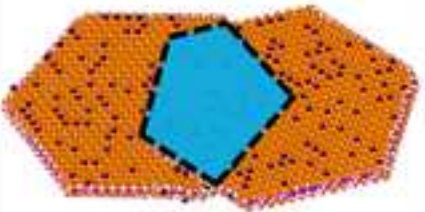
Adapted from P. Aminpour and K. J. Sjoblom (2019). Copyright 2019 ICE Publishing



(d) All-atomic model

Adapted from H. R. Ahmed and S. N. Abduljawad (2017). Copyright 2017 ICE Publishing



Vertex - Vertex	Vertex - Edge	Vertex - Face
		
Edge - Edge		
Type I (full contact)	Type II (partial contact)	Type III (point contact)
		
Edge - Face		Face - Face
Type I (full contact)	Type II (partial contact)	
		

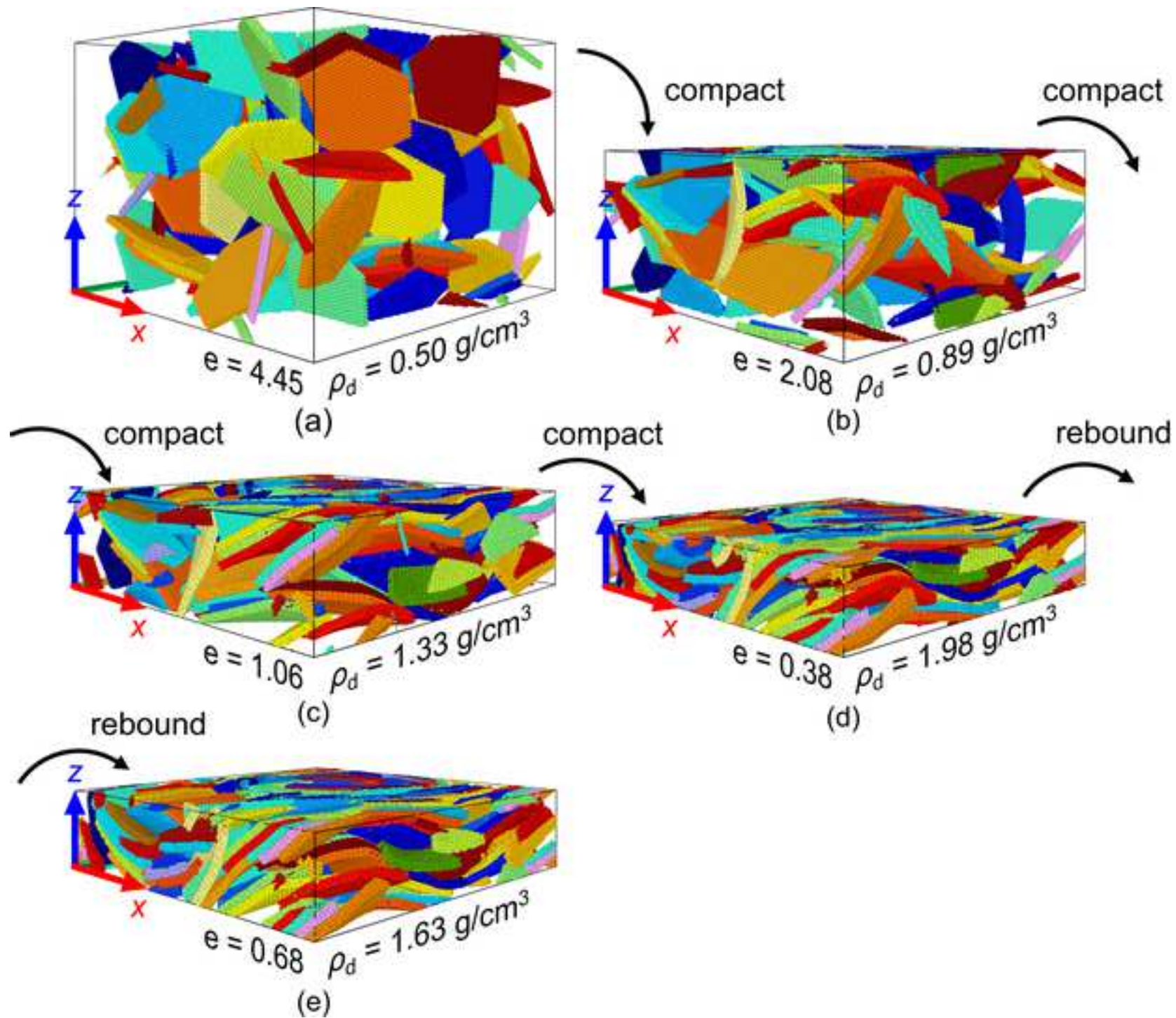
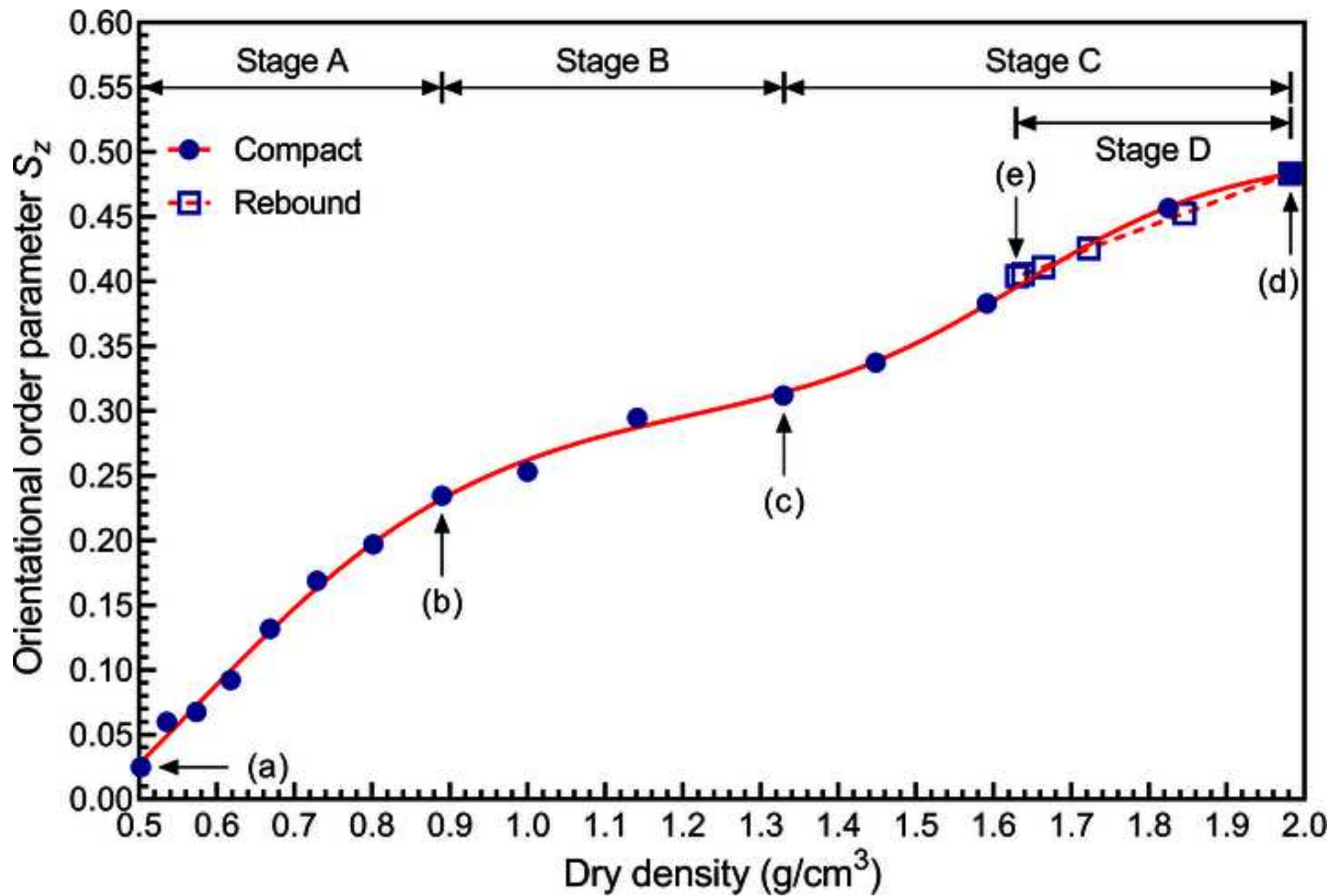
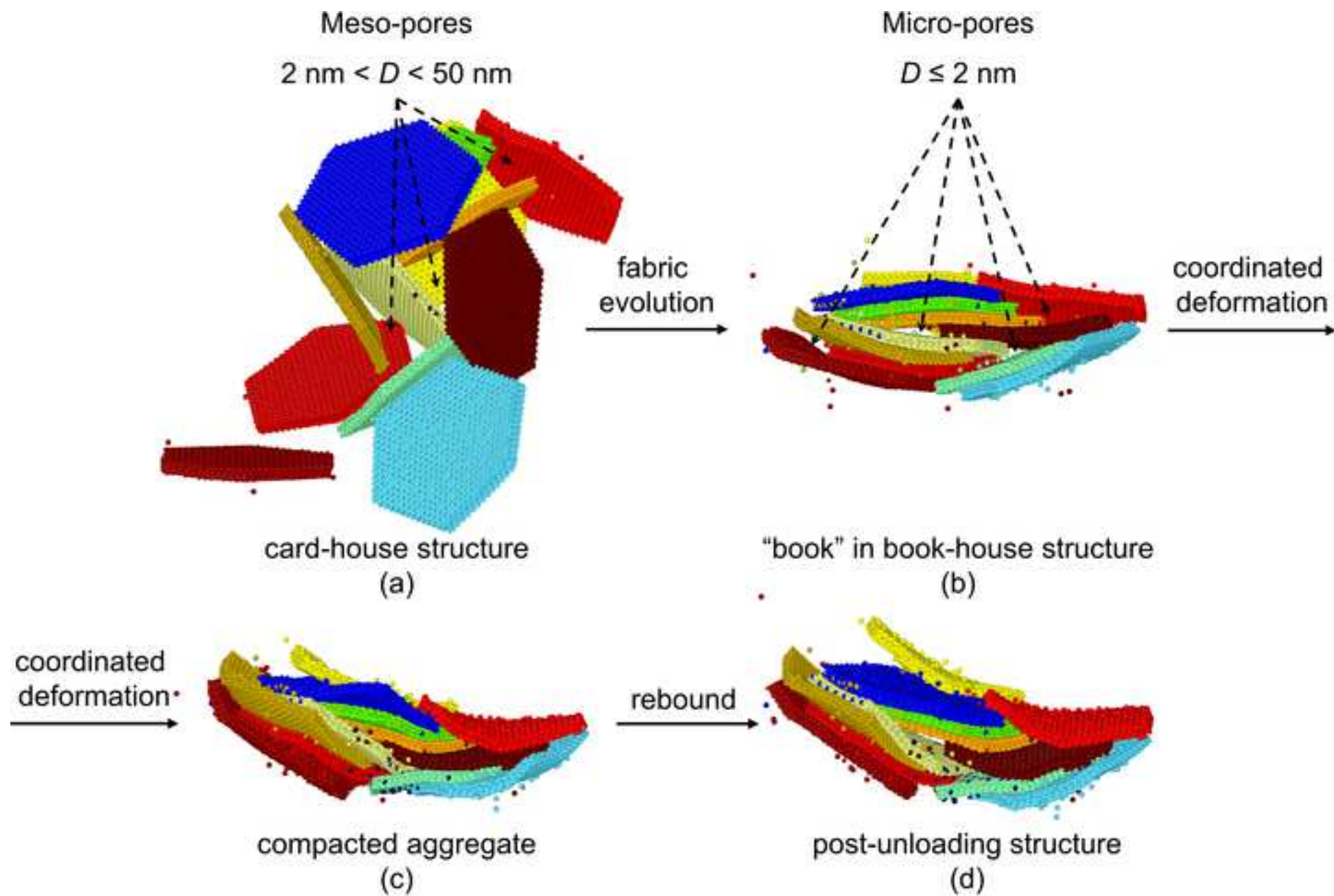


Figure 5





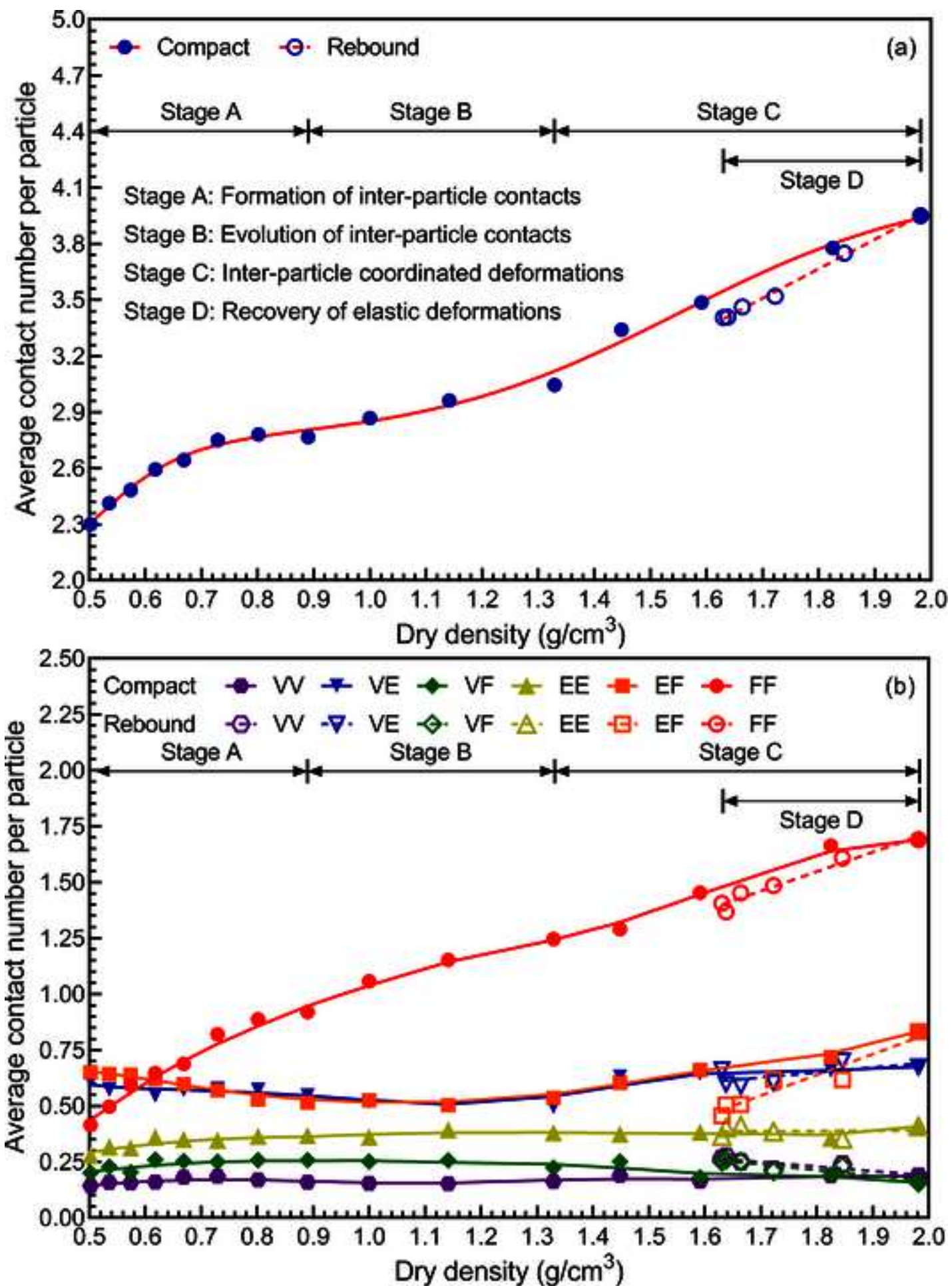


Figure 8

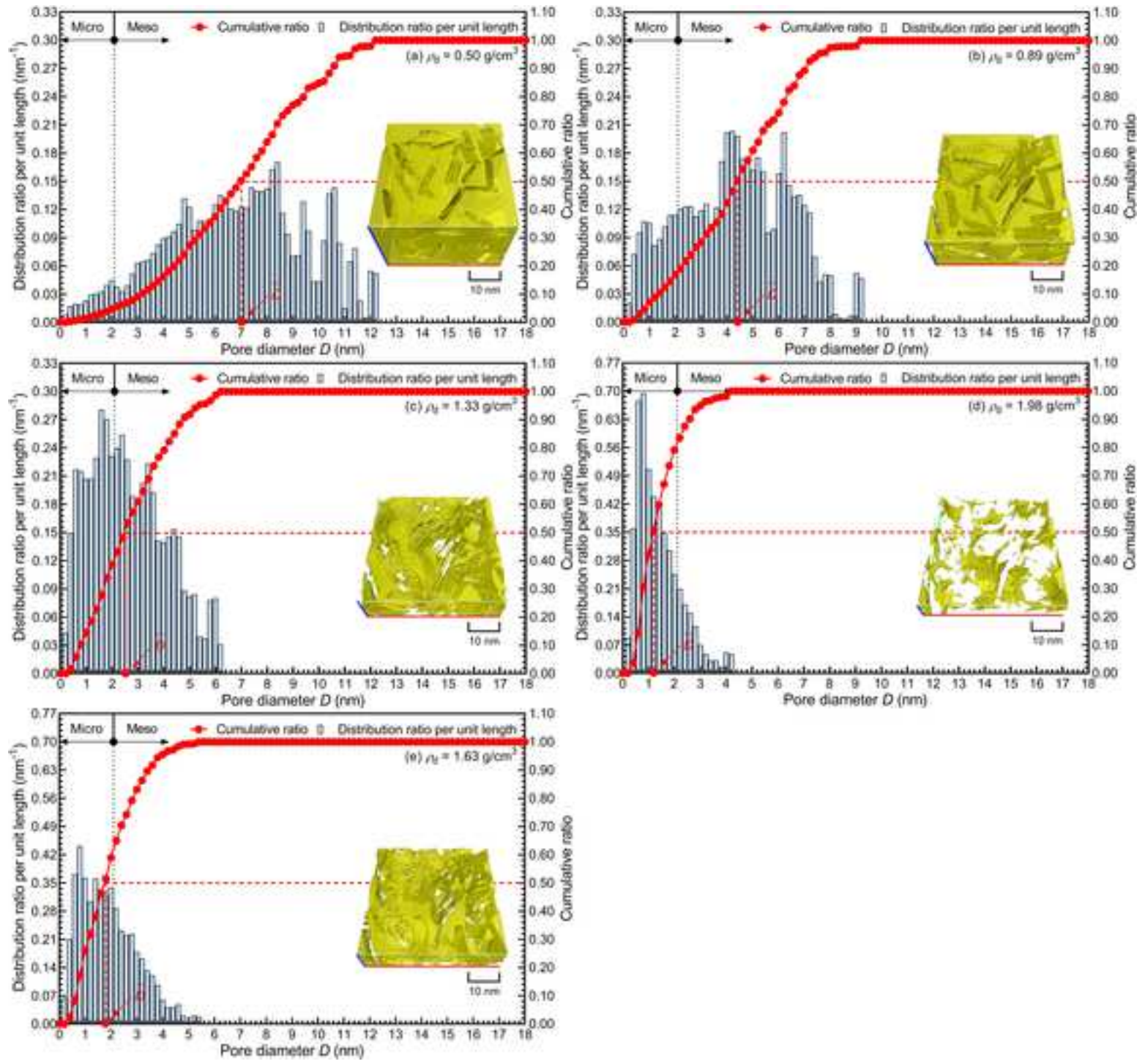
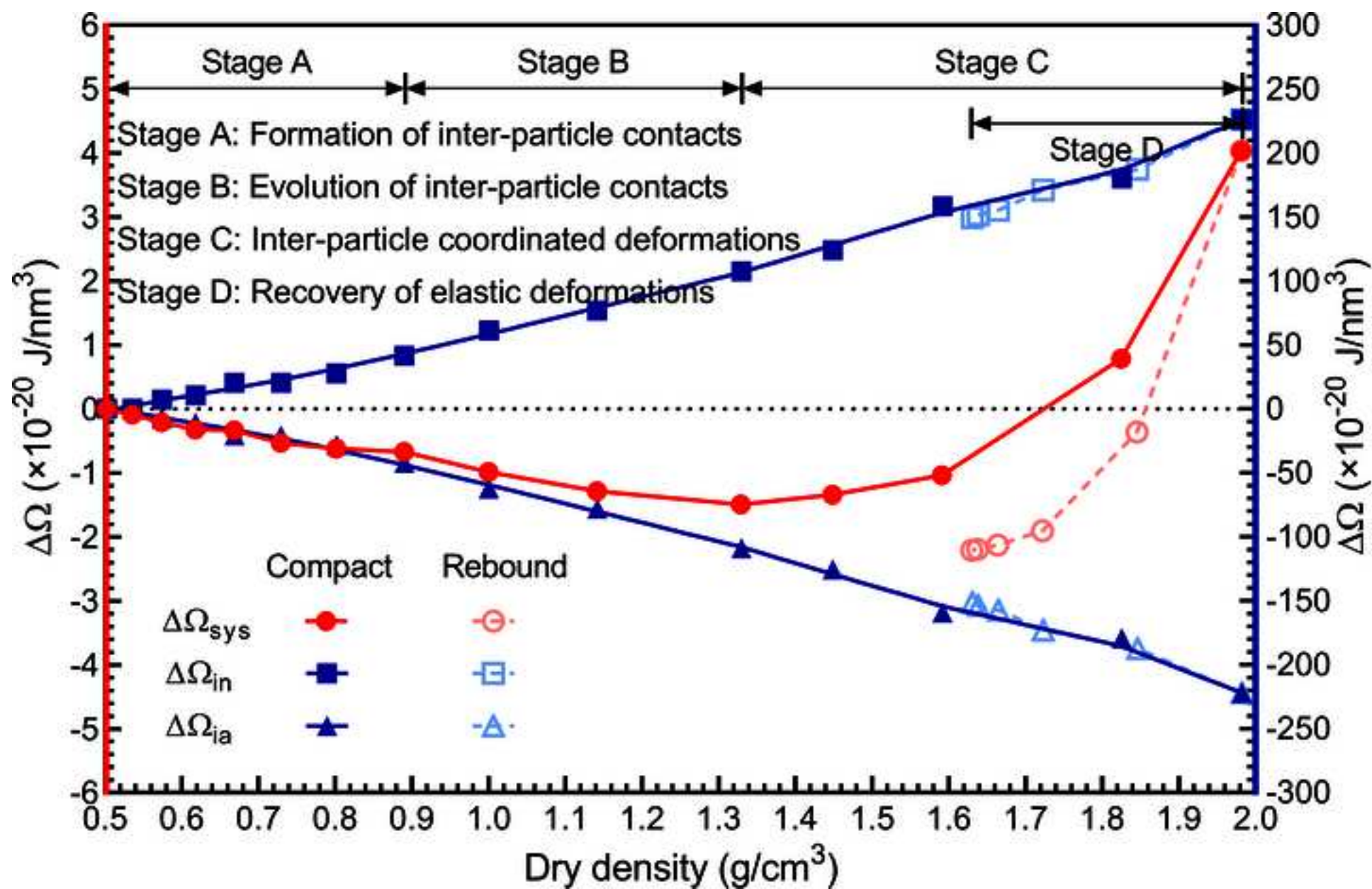
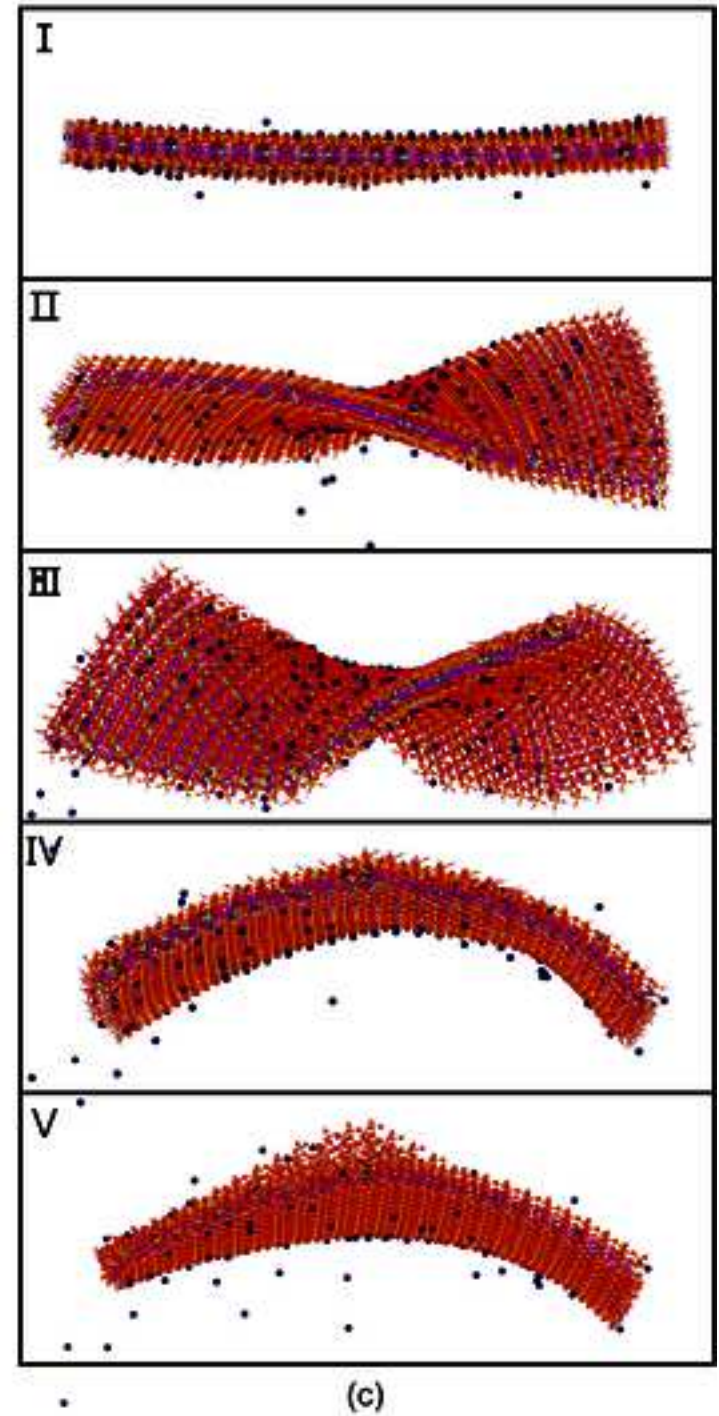
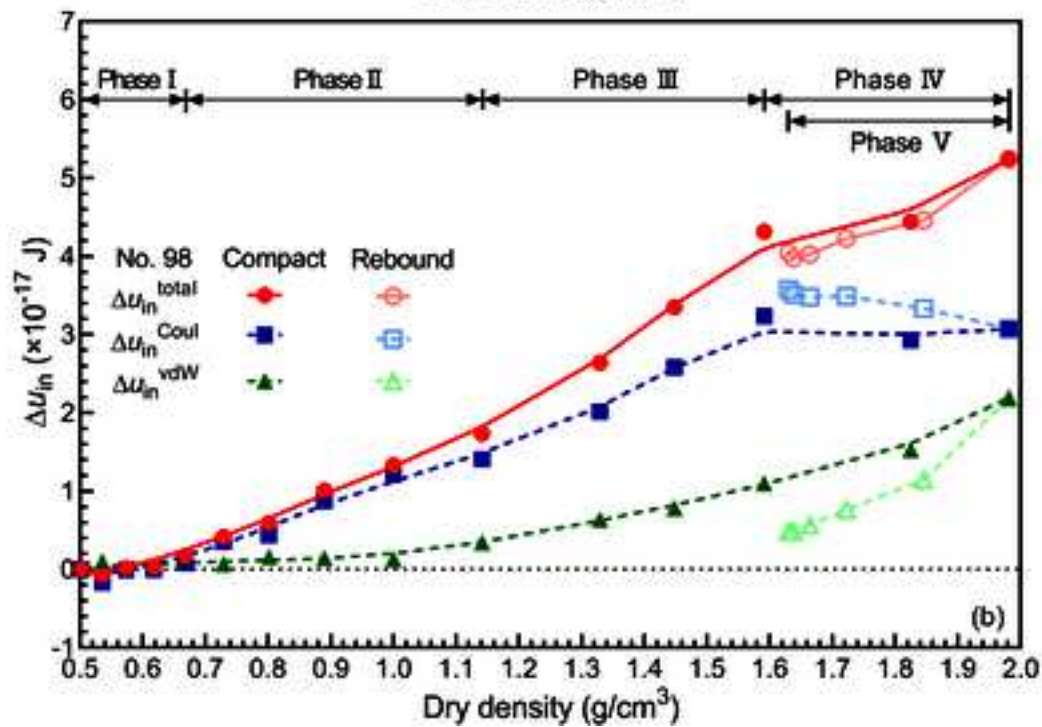
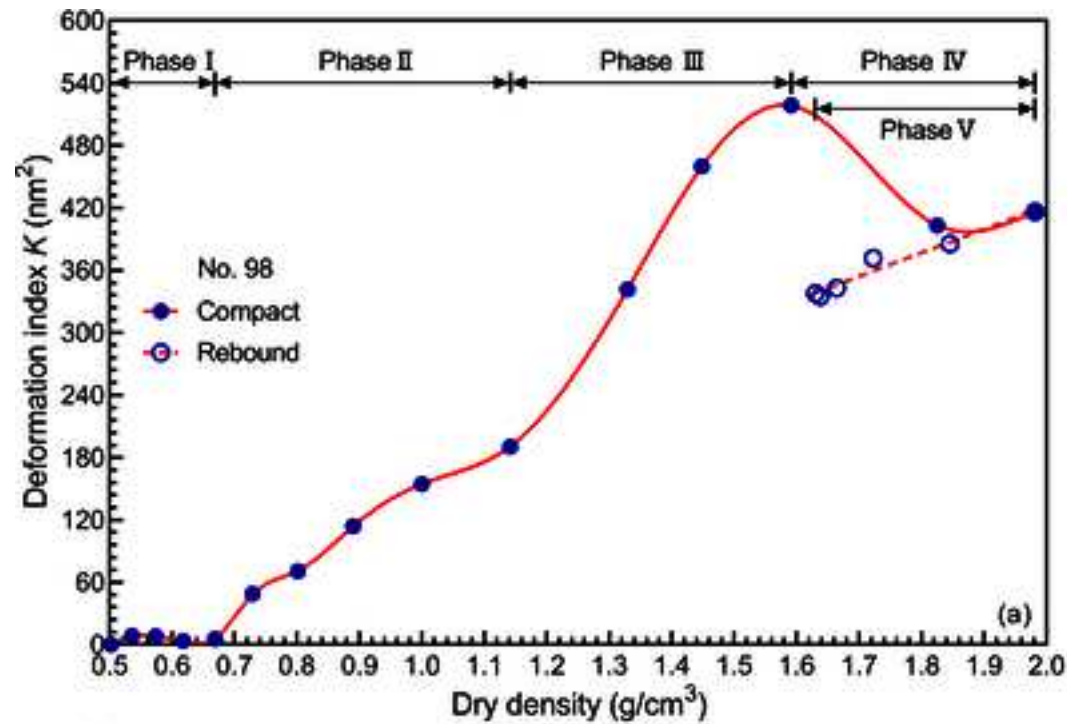
[Click here to access/download;Figure;Figure 8. PSD.tif](#)

Figure 9





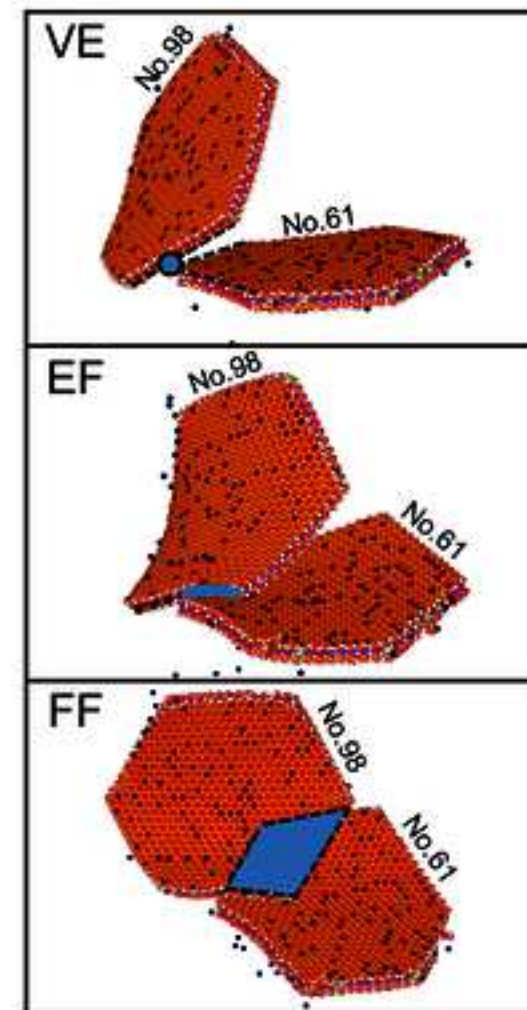
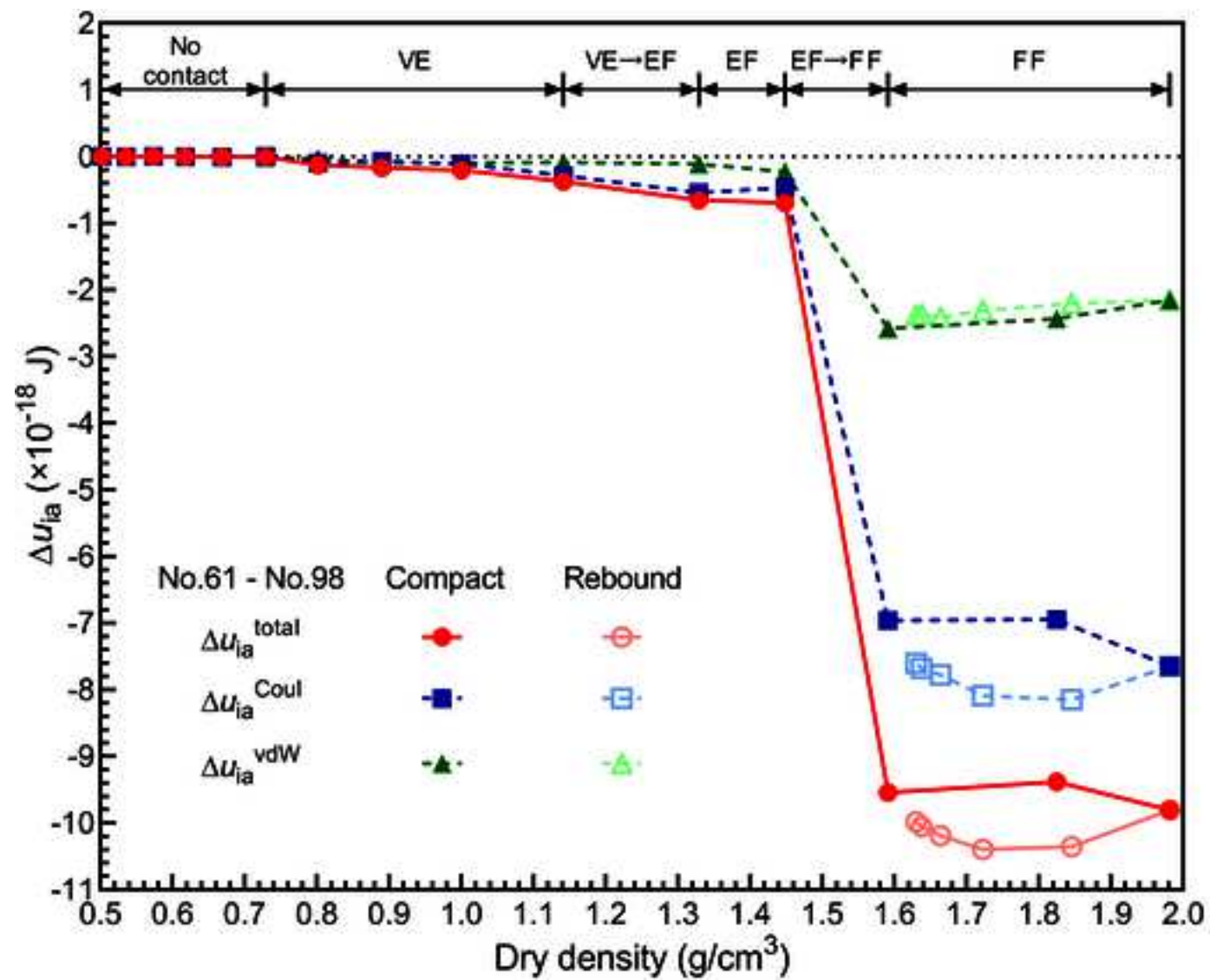


Figure Caption List

Fig. 1. Schematic simulation models of clays adaptive from previous researches. (a) 2D-line discrete element model (Anandarajah 1994); (b) Ellipsoidal particle model (Ebrahimi et al. 2014); (c) United-bead particle model (Aminpour and Sjoblom 2019); (d) All-atomic model (Ahmed and Abduljawad 2017).

Fig. 2. Molecular models for clay particles and their initial assemblage. (a) All-atomic model for a single clay particle; (b) Initial loose packing of 100 particles.

Fig. 3. Diagram of different types of inter-particle contacts. Blue represents the contact point, line or area.

Fig. 4. Snapshots of typical states of the whole system during the compact-rebound process.

Fig. 5. Variation curve of orientation order parameter S_z with dry density.

Fig. 6. Snapshots of the evolution of local clay fabric of 12 clay particles during the compact-rebound process.

Fig. 7. Variations of average number of (a) total contacts and (b) various types of contacts per particle during the compact-rebound process.

Fig. 8. Pore size distribution histogram and cumulative curve for simulated clay with (a) $\rho_d = 0.50 \text{ g/cm}^3$, (b) $\rho_d = 0.89 \text{ g/cm}^3$, (c) $\rho_d = 1.33 \text{ g/cm}^3$, (d) $\rho_d = 1.98 \text{ g/cm}^3$ and (e) $\rho_d = 1.63 \text{ g/cm}^3$ (post-unloading). Insets are the pore space of the simulated clay with corresponding dry densities.

Fig. 9. Variations of potential energy density during the compact-rebound process. Red circles represent ΔQ_{sys} plotting on the left y-axis, blue squares represent ΔQ_{in} plotting on the right y-axis, and blue triangles represent plotting on the right y-axis.

Fig. 10. Variations of particle No.98 in (a) deformation index K , (b) internal potential energy and (c) representative deformation snapshots.

Fig. 11. Variations in interaction potential energy between particles No.61 and No.98.



Click here to access/download
Supplemental Materials File
Compaction-rebound.mp4





Click here to access/download
Supplemental Materials File
Supplementary Materials.docx

